

REPORT DOCUMENTATION PAGE

Public reporting burden for this collection of information is estimated to average 1 hour per response, including the time for reviewing the collection of information, sending the data needed, and completing and reviewing the collection of information. Send no information, including suggestions for reducing this burden, to Washington Headquarters Services, Directorate for Information Operations and Reports, 1204, Arlington, VA 22202-4302, and to the Office of Management and Budget, Paperwork Reduction Project (0704-0188).

AFRL-SR-BL-TR-98-

0084

es, gathering
collection of
ghway, Suite

1. AGENCY USE ONLY (Leave Blank)	2. REPORT DATE 29 Apr 97	3. RE Final (01 Aug 96 - 31 Jan 97)
4. TITLE AND SUBTITLE Focused Application Software for Ferrite Patch Antennas		5. FUNDING NUMBERS F49620-96-C-0029 SBIR Topic AF96-003
6. AUTHORS Dr. Leo Kempel, Mr. Rene Guidry, Mr. Jeff Tackett, Mr. Chris McCool, Mr. Arik Brown, Dr. John Volakis		
7. PERFORMING ORGANIZATION NAME(S) AND ADDRESS(ES) Mission Research Corporation University of Michigan Valparaiso, FL 32580 Ann Arbor, MI 48109-2122		8. PERFORMING ORGANIZATION REPORT NUMBER MRC C-96095
9. SPONSORING/MONITORING AGENCY NAME(S) AND ADDRESS(ES) AFOSR/NM 110 Duncan Avenue, Room B-115 Bolling Air Force Base, DC 20332-8080		10. SPONSORING/MONITORING AGENCY REPORT NUMBER
11. SUPPLEMENTARY NOTES		
12a. DISTRIBUTION AVAILABILITY STATEMENT Approved for Public Release		12b. DISTRIBUTION CODE
13. ABSTRACT (Maximum 200 words) During Phase I of this SBIR effort, MRC and UM demonstrated the feasibility of using modern finite element analysis to characterize the behavior of ferrite materials. Specifically, MRC and UM investigated the following: 1. Finite element formulations for ferrite materials. 2. Implementation of those formulas in a computer program. 3. Convergence issues when ferrite materials are being modeled. 4. Mesh truncation schemes. 5. Element distortion effects. 6. And uses of ferrite antennas as frequency-agile antennas, polarization-agile antennas and electronic shutter radomes.		
14. SUBJECT TERMS behavior, ferrite, antennas		15. NUMBER OF PAGES
16. PRICE CODE		
17. SECURITY CLASSIFICATION OF REPORT Unclassified	18. SECURITY CLASSIFICATION OF THIS PAGE Unclassified	19. SECURITY CLASSIFICATION OF ABSTRACT Unclassified
20. LIMITATION OF ABSTRACT UL		

DIS QUALITY PRODUCT 2

19980129 019

Focused Application Software for Ferrite Patch Antennas

R&D Final Report for Phase I SBIR

Reporting Period: 1 August 1996 to 30 April 1997

Contract Number: F49620-96-C-0029

SBIR Topic: AF96-003

MRC Project: 96095

Prepared by:	Dr. Leo C. Kempel, Mr. Rene Guidry	Mr. Arik Brown, Dr. John Volakis
	Mr. Jeff Tackett, Mr. Chris McCool	Radiation Laboratory
	Mission Research Corporation	University of Michigan
	147 John Sims Parkway	1301 Beal Ave
	Valparaiso, FL 32580	Ann Arbor, MI 48109-2122

"Distribution is authorized to DoD agencies only, as the data is PROPRIETARY (see section 5.8 of DoD SBIR program solicitation 96.1)." Requests for release shall be referred to AFOSR/NM.

"WARNING EXPORT CONTROL ACT (Title 22, USC SEC 2751 et seq.) or EXPORT Administration Act of 1979, as amended, Title 50, USC app 2401, et seq. Violations of these laws are subject to severe criminal penalties. Disseminate in accordance with the provisions of DoD Directive 5230.25.

Table of Contents

A. BACKGROUND	4
B. FINITE ELEMENT FORMULATION FOR ANISOTROPIC MATERIALS.....	5
B.1 GENERAL FINITE ELEMENT FORMULATION FOR ANISOTROPIC MATERIALS	5
B.2 FINITE ELEMENT-BOUNDARY INTEGRAL FORMULATION FOR ANISOTROPIC MATERIALS	7
B.3 FINITE ELEMENT METHOD USING BRICK ELEMENTS FOR ANISOTROPIC MATERIALS	9
<i>B.3.1 Anisotropic Brick Element Matrices.....</i>	<i>10</i>
<i>B.3.2 Boundary Integral Matrix Entries.....</i>	<i>12</i>
C. FERRITE MATERIAL MODEL.....	14
D. VALIDATION.....	17
D.1 CAVITY-BACKED APERTURES	19
D.2 PATCH ANTENNAS.....	21
E. CONVERGENCE ISSUES.....	22
E.1 PROPAGATION CONSTANTS	22
<i>E.1.1 Ferrite Cavity Example.....</i>	<i>23</i>
<i>E.1.2 Ferrite Cavity with Patch Antenna Example.....</i>	<i>26</i>
F. PHASE I TRADE STUDIES	29
F.1 PERFECTLY MATCH LAYER MESH TRUNCATION	29
<i>F.1.1 Curved PML Trade Study.....</i>	<i>30</i>
F.2 MATRIX ITERATIVE SOLVERS AND CONDITIONING	31
F.3 ELEMENT DISTORTION.....	33
G. FERRITE-BACKED PATCH ANTENNA EXAMPLES.....	34
G.1 RADIATION PROPERTIES OF A SINGLE FERRITE-BACKED PATCH ANTENNA	35
<i>G.1.1 Dielectric-backed Patch Antenna.....</i>	<i>36</i>
<i>G.1.2 X-axis Ferrite Biasing</i>	<i>36</i>
<i>G.1.3 Y-axis Ferrite Biasing.....</i>	<i>37</i>
<i>G.1.4 Z-axis Ferrite Biasing.....</i>	<i>38</i>
<i>G.1.5 Summary of Radiation Simulations</i>	<i>40</i>
G.2 LARGE FERRITE-BACKED ANTENNA ARRAY	40
H. NON-UNIFORM STATIC BIAS FIELD EFFECTS.....	41
I. FERRITE RADOMES: AN ELECTRONIC SHUTTER CONCEPT.....	43
I.1 TWO APERTURE FE-BI COMPUTER PROGRAM FOR TRANSMISSION CALCULATIONS.....	43
I.2 TRANSMISSION COEFFICIENT CALCULATIONS	43
J. CONCLUDING REMARKS AND SUGGESTIONS FOR FUTURE WORK.....	44
J.1 SUGGESTIONS FOR FUTURE WORK	44
K. REFERENCES.....	45

Table of Figures

FIGURE B-1. ILLUSTRATION OF THE COMPUTATIONAL VOLUME (V), BOUNDING SURFACE (S), AND SURFACE AT WHICH THE RADIATION CONDITION IS APPLIED (S_0)	6
FIGURE B-2. ILLUSTRATION OF A CAVITY-BACKED APERTURE LOCATED IN AN INFINITE GROUND PLANE	8
FIGURE B-3. VARIOUS FINITE ELEMENT SHAPES	9
FIGURE B-4. BRICK FINITE ELEMENT ILLUSTRATING THE SIX NODES AND TWELVE EDGES THAT FORM THE BRICK	10
FIGURE C-1. ILLUSTRATION OF MAGNETIC LINE WIDTH (AFTER POZAR[1])	16
FIGURE D-1. AGREEMENT BETWEEN BiCG AND LU DECOMPOSITION SOLVERS	18
FIGURE D-2. LAYERED CAVITY-BACKED APERTURE USED FOR COMPARISON BETWEEN MoM AND FE-BI	19
FIGURE D-3. REPRODUCTION OF FIGURE 6.1 IN [2]	19
FIGURE D-4. MRC'S FE-BI COMPARISON TO FIGURE D-3	20
FIGURE D-5. CONDITION NUMBER VERSUS FREQUENCY (LARGE CONDITION NUMBERS INDICATE A POORLY CONDITIONED MATRIX)	21
FIGURE D-6. REPRODUCTION OF POZAR'S [3] RESULTS	21
FIGURE D-7. SCATTERING BY A 1.3x1.3 CM PATCH ANTENNA RECESSED IN A 2.6x2.6x0.13 CM FERRITE FILLED CAVITY	22
FIGURE E-1. FERRITE CAVITY GEOMETRY	23
FIGURE E-2. μ vs. f , $H_0 = 100$ Oe, $4\pi M_s = 800$ G, $\Delta H = 10$ Oe	24
FIGURE E-3. κ vs. f , $H_0 = 100$ Oe, $4\pi M_s = 800$ G, $\Delta H = 10$ Oe	24
FIGURE E-4. α NORMALIZED TO k_0 , $-\mu_{\text{eff}} = \frac{\mu^2 - \kappa^2}{\mu}$, $--\mu_{\text{eff}} = \mu + \kappa$, $-\cdot\mu_{\text{eff}} = \mu - \kappa$	25
FIGURE E-5. β NORMALIZED TO k_0 , $-\mu_{\text{eff}} = \frac{\mu^2 - \kappa^2}{\mu}$, $--\mu_{\text{eff}} = \mu + \kappa$, $-\cdot\mu_{\text{eff}} = \mu - \kappa$	25
FIGURE E-6. CONVERGENCE PERFORMANCE, $H_0 = 100$ Oe, # OF UNKNOWNNS = 3915	26
FIGURE E-7. μ vs. f , $H_0 = 600$ Oe, $4\pi M_s = 650$ G, $\Delta H = 30$ Oe	26
FIGURE E-8. κ vs. f , $H_0 = 600$ Oe, $4\pi M_s = 650$ G, $\Delta H = 30$ Oe	27
FIGURE E-9. α NORMALIZED TO k_0 , $-\mu_{\text{eff}} = \frac{\mu^2 - \kappa^2}{\mu}$, $--\mu_{\text{eff}} = \mu + \kappa$, $-\cdot\mu_{\text{eff}} = \mu - \kappa$	27
FIGURE E-10. β NORMALIZED TO k_0 , $-\mu_{\text{eff}} = \frac{\mu^2 - \kappa^2}{\mu}$, $--\mu_{\text{eff}} = \mu + \kappa$, $-\cdot\mu_{\text{eff}} = \mu - \kappa$	28
FIGURE E-11. CONVERGENCE PERFORMANCE, $H_0 = 100$ Oe, # OF UNKNOWNNS = 3766	28
FIGURE F-1. COMPARISON OF NEW ANISOTROPIC PML AND TRADITIONAL PML	29
FIGURE F-2. PML ABSORBER DESIGN CURVES WHERE $\beta t/\lambda_0$ IS THE THICKNESS OF THE PML AND N IS A PML PARAMETER DESCRIBING THE MATERIAL PROPERTIES. THE STRAIGHT LINES GIVE $ R $ IN DB AND THE CURVED LINES GIVE N: (—) EXACT $ R $, (···) HOMOGENEOUS CASE AND (— · —) INHOMOGENEOUS CASE	30
FIGURE F-3. RESULTS OF THE CURVED PML TRADE STUDY	31
FIGURE F-4. CONVERGENCE BEHAVIOR FOR THREE ITERATIVE SOLVERS (3000 UNKNOWNNS)	32
FIGURE F-5. CONVERGENCE BEHAVIOR OF AN ITERATIVE SOLUTION WITH AND WITHOUT PRECONDITIONING	32
FIGURE F-6. ELEMENT DISTORTION CASES EXAMINED (DATA SHOWN IN FIGURE F-7)	33
FIGURE F-7. EFFECT OF ELEMENT DISTORTION ON MATRIX CONDITION NUMBER. THE CASES CORRESPOND TO THE FOUR BRICK IMAGES SHOWN IN FIGURE F-6	34
FIGURE G-1. FIGURE 2 FROM POZAR'S PAPER [3]. THIS ILLUSTRATES THE VARIATION OF BIAS FREQUENCY AS THE BIAS FIELD STRENGTH IS CHANGED FOR A NORMALLY BIASED FERRITE-BACKED PATCH ANTENNA	35
FIGURE G-2. IMPEDANCE SPECTRUM OF A 0.61x0.61 CM DIELECTRIC-BACKED PATCH ANTENNA	36
FIGURE G-3. IMPEDANCE SPECTRUM FOR A 0.61x0.61 CM PATCH PRINTED ON A X-AXIS BIASED FERRITE	37

FIGURE G-4. IMPEDANCE SPECTRUM OF A 0.61x0.61 CM PATCH ANTENNA ON A Y-BIASED FERRITE.....	38
FIGURE G-5. IMPEDANCE SPECTRUM FOR A 0.61x0.61 CM ANTENNA ON A NORMALLY BIASED FERRITE.....	38
FIGURE G-6. GAIN PATTERN FOR A NORMALLY BIASED PATCH ANTENNA AT 5.115 GHZ.	39
FIGURE G-7. GAIN PATTERN FOR A NORMALLY BIASED PATCH ANTENNA AT 6.445 GHZ.	39
FIGURE G-8. RADIATION PATTERN FROM AN 11 X 11 ARRAY OF PATCH ANTENNAS PRINTED ON A FERRITE SUBSTRATE. <i>THIS EXAMPLE ILLUSTRATES MRC'S ABILITY TO MODEL LARGE STRUCTURES ON FERRITE MATERIALS INCLUDING ANTENNA ELEMENTS AND PHASE SHIFTING DEVICES.</i>	41
FIGURE H-1. MEASURED MAGNETIC FIELD DISTRIBUTION WITHIN CAVITY FROM [2].	42
FIGURE H-2. ILLUSTRATION OF NON-UNIFORM BIAS FIELD EFFECT ON THE RCS OF A FERRITE-FILLED CAVITY.....	42
FIGURE I-1. TRANSMISSION COEFFICIENT FOR A FERRITE SUBSTRATE UNDER VARIOUS BIAS CONDITIONS.	44

A. Background

Under this Phase I SBIR effort, Mission Research Corporation (MRC) and the University of Michigan (UM) undertook a feasibility study involving the application of recent innovations in the finite element (FE) method to the problem of modeling conformal antennas that utilize ferrite materials. This final technical report presents a comprehensive technical summary of the work undertaken during Phase I.

Ferrite materials have been suggested by members of the antenna community as a unique antenna loading material primarily due to its tunable electrical properties. In particular, by appropriate application of a static magnetic bias field, a ferrite sample can exhibit a wide variety of electrical properties from nearly transparent to nearly opaque without any mechanical intervention. Ferrites can also be magnetically tuned to preferentially interact with a given electromagnetic field polarization. For example, the sample can appear to be opaque to one polarization while transparent to the orthogonal polarization. Such properties can be exploited by antenna and low observable (LO) designers. In this report, preliminary research concerning such properties will be presented.

One difficulty in designing such antennas involves the dearth of appropriate analysis and design tools. Traditional analysis methods, utilizing the popular method of moments (MoM) procedure (i.e. integral equations), have proven unsatisfactory, principally due to the fact that the static magnetic field cannot be properly represented using typical MoM techniques. Practical biasing magnets produce a non-uniform static magnetic field and hence the ferrite sample, though physically homogeneous, appears to be electrically inhomogeneous. Volume MoM analysis programs, which can indeed model such electrical inhomogeneities, are inefficient and difficult to formulate and program for anisotropic materials such as ferrites.

The finite element method is uniquely suitable for analyzing the properties of ferrite materials. This is due to the fact that the finite element method is typically formulated in the frequency domain, and hence can readily accommodate the frequency-dependent properties of ferrites. In addition, since the finite element method requires no Green's function for the ferrite volume, its formulation and implementation is particularly easy. Also, since the finite element method is based on partial differential equations (PDE), it possesses a locality property in that only field expansions in the near vicinity of one another couple directly. All of these features lead to the conclusion that the finite element method is well-suited for ferrite material modeling.

The focus of this Phase I SBIR topic involves the investigation as to whether the FE method can be used to model ferrite-loaded antennas. In addition, it seeks to begin to answer the question, "What are the advantages and disadvantages of ferrite-loaded antenna?" Note that in this report, a ferrite-loaded antenna does not include the ferrite bead loads commonly used to alter the performance of certain antennas. Rather, the ferrite load is either a substrate or superstrate material.

In this report, the finite element method will be shown to be well-suited for ferrite antenna analysis. Also, novel uses of such antennas will be explored including:

1. Frequency agile antennas.
2. Polarization agile antennas.
3. Radar cross section (RCS) reduction techniques.

We begin this report with the finite element formulation for ferrite materials followed by a discussion of MRC's and UM's efforts during Phase I.

B. Finite Element Formulation for Anisotropic Materials

The finite element formulation presented herein is very general. It does not assume any particular element shape, expansion (or shape) function, or mesh termination condition. For practical analysis, the formulation will need to be specialized. Since during Phase I, both MRC and UM utilized brick elements and a boundary integral (BI) mesh closure, these special cases will be presented following the general discussion. Note that both MRC and UM chose to use bricks and a BI termination to leverage previous work and thus be able to quickly investigate the special properties, features, and challenges associated with ferrite materials. A more general treatment is planned for Phase II.

B.1 General Finite Element Formulation for Anisotropic Materials

The finite element formulation begins with Maxwell's equations

$$\nabla \times \mathbf{E}^{\text{int}} = -jk_0 Z_0 \bar{\bar{\mu}}_r \mathbf{H}^{\text{int}} \quad (1)$$

$$\nabla \times \mathbf{H}^{\text{int}} = +jk_0 Z_0 \bar{\bar{\epsilon}}_r \mathbf{E}^{\text{int}} \quad (2)$$

where the interior (e.g. within the computational volume) electric and magnetic fields are denoted by \mathbf{E}^{int} and \mathbf{H}^{int} , respectively. The relative permittivity ($\bar{\bar{\epsilon}}_r$) and permeability ($\bar{\bar{\mu}}_r$) are tensors and can vary on an element-by-element basis within the computational volume. The free-space wavenumber and impedance are denoted by $k_0 = \omega \sqrt{\mu_0 \epsilon_0}$ and $Z_0 = \sqrt{\mu_0 / \epsilon_0}$, respectively, where the free-space permittivity and permeability are represented by ϵ_0 and μ_0 , respectively. Pre-multiplying (1) by the inverse permeability tensor ($\bar{\bar{\mu}}_r^{-1}$), taking the curl of (1) and utilizing (2), the second-order PDE is obtained

$$\nabla \times [\bar{\bar{\mu}}_r^{-1} \cdot \nabla \times \mathbf{E}^{\text{int}}] - k_0^2 \bar{\bar{\epsilon}}_r \cdot \mathbf{E}^{\text{int}} = -[jk_0 Z_0 \mathbf{J}^{\text{imp}} + \nabla \times (\bar{\bar{\mu}}_r^{-1} \cdot \mathbf{M}^{\text{imp}})] \quad (3)$$

This is the vector wave equation in terms of the total electric field within the computational volume, V which is illustrated in Figure B-1. In (3), \mathbf{J}^{imp} and \mathbf{M}^{imp} are the impressed electric and magnetic current within the computational volume, respectively.

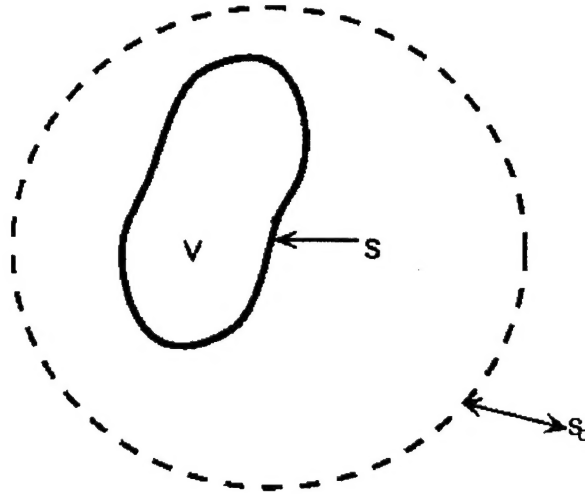


Figure B-1. Illustration of the computational volume (V), bounding surface (S), and surface at which the radiation condition is applied (S_0).

Throughout this report, total electric fields will be the unknowns since the BI mesh closure used during Phase I involved a half space Green's function (e.g. cavities recessed in an infinite metallic plane) and hence a total magnetic field formulation is impractical. This is not to say that a magnetic field formulation will not be preferable for ferrite materials. Indeed, the fact that a magnetic field formulation precludes the need for an inverse permeability tensor ($\bar{\bar{\mu}}_r^{-1}$) is desirable due to singularities in that tensor near the forced precession frequency. Hence, during Phase II it will be important to examine the benefits of a magnetic field formulation utilizing an artificial mesh termination condition such as perfectly matched layers (PML).

Two methods are typically used to convert the continuous domain wave equation represented by (3) and a discrete approximation that can be solved on a digital computer, namely: the method of functionals and method of weighted residuals. Throughout this report, the method of weighted residuals will be used principally due to the fact that it is familiar to electrical engineers who have used the method of moments before. The method of weighted residuals begins by multiplying (3) with an, as of yet arbitrary, weight function (W_i^e) that has support only over one finite element (e). There are N such unique weights corresponding to the number of unknowns in the final system. After multiplication, (3) is integrated over the entire computational volume (though of course the finite support of the weight functions will limit the integration to the element associated with the weight function) to get

$$\begin{aligned} \int_V \left\{ W_i^e \cdot \nabla \times [\bar{\bar{\mu}}_r^{-1} \cdot \nabla \times \mathbf{E}^{int}] - k_0^2 W_i^e \cdot \bar{\bar{\epsilon}}_r \cdot \mathbf{E}^{int} \right\} dV = \\ - \int_V W_i^e \cdot [jk_0 Z_0 \mathbf{J}^{imp} + \nabla \times (\bar{\bar{\mu}}_r^{-1} \cdot \mathbf{M}^{imp})] dV = f_i^{e,int} \end{aligned} \quad (4)$$

where the right-hand side (interior excitation) is represented by $f_i^{e,int}$ for the remainder of this report. This equation is not convenient for solution since the electric field receives two derivatives and the resulting formulation is unsymmetric. Therefore, it is advantageous to transfer one derivative from

the unknown electric field to the weight function in the first integrand using the first vector Green's theorem

$$\int_V \mathbf{W}_i^e \cdot \nabla \times \left[\bar{\bar{\mu}}_r^{-1} \cdot \nabla \times \mathbf{E}^{int} \right] dV = \int_V \left(\nabla \times \mathbf{W}_i^e \right) \cdot \left(\bar{\bar{\mu}}_r^{-1} \cdot \nabla \times \mathbf{E}^{int} \right) dV - \oint_S \hat{\mathbf{n}} \cdot \left(\mathbf{W}_i^e \times \left[\bar{\bar{\mu}}_r^{-1} \cdot \nabla \times \mathbf{E}^{int} \right] \right) dS \quad (5)$$

Using (1) and a vector triple product, (5) becomes

$$\int_V \mathbf{W}_i^e \cdot \nabla \times \left[\bar{\bar{\mu}}_r^{-1} \cdot \nabla \times \mathbf{E}^{int} \right] dV = \int_V \left(\nabla \times \mathbf{W}_i^e \right) \cdot \left(\bar{\bar{\mu}}_r^{-1} \cdot \nabla \times \mathbf{E}^{int} \right) dV - jk_0 Z_0 \oint_S \mathbf{W}_i^e \cdot (\hat{\mathbf{n}} \times \mathbf{H}^{int}) dS \quad (6)$$

In this, the surface term relates the tangential electric field (\mathbf{W}_i^e) with the tangential magnetic field ($\hat{\mathbf{n}} \times \mathbf{H}^{int}$) on the surface enclosing the volume (V) where $\hat{\mathbf{n}}$ is the outward directed normal to the surface S (∂V). Using (6) in (4), the weak-form of the vector wave equation is obtained

$$\int_V \left[\left(\nabla \times \mathbf{W}_i^e \right) \cdot \bar{\bar{\mu}}_r^{-1} \cdot \left(\nabla \times \mathbf{E}^{int} \right) - k_0^2 \mathbf{W}_i^e \cdot \bar{\bar{\epsilon}}_r \cdot \mathbf{E}^{int} \right] dV - jk_0 Z_0 \oint_S \mathbf{W}_i^e \cdot (\hat{\mathbf{n}} \times \mathbf{H}^{int}) dS = f_i^{e,int} \quad (7)$$

This equation satisfies (3) in the weak or integrated sense rather than at every point within the computational volume.

Finite element programs are typically divided into two groups based upon how the surface magnetic field is related to the surface electric field:

1. locally through a approximate condition such as absorbing boundary conditions (ABC) or perfectly matched layers (PML), or
2. globally via a boundary integral involving a dyadic Green's function for the external region.

During Phase I, both MRC and UM used the later approach and its formulation will be presented next.

B.2 Finite Element-Boundary Integral Formulation for Anisotropic Materials

The finite element-boundary integral formulation begins by postulating a magnetic field integral equation (MFIE) for the exterior region such as

$$\frac{\hat{\mathbf{n}} \times \mathbf{H}^{ext}(\mathbf{r})}{2} - \oint_S \left[\hat{\mathbf{n}} \times \left(\nabla \times \bar{\bar{G}} \cdot \hat{\mathbf{n}}' \times \mathbf{H}^{ext}(\mathbf{r}') \right) \right] dS' - jk_0 Y_0 \oint_S \left[\hat{\mathbf{n}} \times \bar{\bar{G}} \cdot \hat{\mathbf{n}}' \times \mathbf{E}^{ext}(\mathbf{r}') \right] dS = \hat{\mathbf{n}} \times \left[\mathbf{H}^{inc}(\mathbf{r}) + \mathbf{H}^{ref}(\mathbf{r}) \right] \quad (8)$$

where the field quantities are now in the exterior region (e.g. between S and S_0 in Figure B-1), the prime variable (\mathbf{r}') refer to the source point while the unprimed variable (\mathbf{r}) refer to the test point, and $Y = 1/Z_0$. The excitation (the right-hand side) is separated in term of an incident magnetic

field (\mathbf{H}^{inc}) and a reflected magnetic field (\mathbf{H}^{ref}). For geometries involving an infinite metallic structure, this field representation is used. For geometries involving finite structures, the reflected field is omitted and for radiation analysis, both the incident and the reflected fields are omitted.

This MFIE is then tested with a separate vector test function (\mathbf{Q}_i^e)

$$\begin{aligned} \frac{1}{2} \oint_S \mathbf{Q}_i^e \cdot \hat{\mathbf{n}} \times \mathbf{H}^{\text{ext}} dS - \oint_S \oint_{S'} \mathbf{Q}_i^e \cdot \hat{\mathbf{n}} \times \left[\nabla \times \overline{\overline{\mathbf{G}}} \cdot \hat{\mathbf{n}}' \times \mathbf{H}^{\text{ext}} \right] dS' dS - \\ jk_0 Y_0 \oint_S \oint_{S'} \mathbf{Q}_i^e \cdot \hat{\mathbf{n}} \times \left[\overline{\overline{\mathbf{G}}} \cdot \hat{\mathbf{n}}' \times \mathbf{E}^{\text{ext}} \right] dS' dS = \oint_S \mathbf{Q}_i^e \cdot \hat{\mathbf{n}} \times \left[\mathbf{H}^{\text{inc}} + \mathbf{H}^{\text{ref}} \right] dS = f_i^{\text{e,ext}} \end{aligned} \quad (9)$$

and the interior and exterior fields are matched across the interface using either point-by-point coupling

$$\hat{\mathbf{n}} \times [\mathbf{E}^{\text{int}} - \mathbf{E}^{\text{ext}}] = 0 \quad \text{and} \quad \hat{\mathbf{n}} \times [\mathbf{H}^{\text{int}} - \mathbf{H}^{\text{ext}}] = 0 \quad (10)$$

or in an average sense

$$\oint_S \mathbf{Q}_i^e \cdot \hat{\mathbf{n}} \times [\mathbf{E}^{\text{int}} - \mathbf{E}^{\text{ext}}] dS = 0 \quad \text{and} \quad \oint_S \mathbf{Q}_i^e \cdot \hat{\mathbf{n}} \times [\mathbf{H}^{\text{int}} - \mathbf{H}^{\text{ext}}] dS = 0 \quad (11)$$

Although the formulation is appropriate for general structures, such as the one illustrated in Figure B-1, for Phase I both MRC and UM used a specialized FE-BI formulation for cavities recessed in an infinite ground plane, such as the one shown in Figure B-2, to save on computer resources.

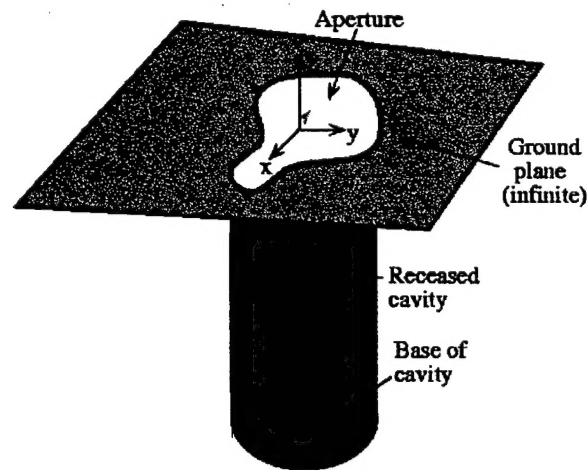


Figure B-2. Illustration of a cavity-backed aperture located in an infinite ground plane.

This is due to the fact that a particularly efficient FE-BI computer program was developed by UM to analyze such structures and using this program, both MRC and UM were able to quickly investigate a large number of ferrite antenna configurations. Such efficiency is important for performing an

exhaustive investigation of ferrite antenna capabilities, idiosyncrasies, and potential. This special formulation allowed the use of

$$\hat{\mathbf{z}} \times \mathbf{H}^{\text{ext}} = \hat{\mathbf{z}} \times [\mathbf{H}^{\text{inc}} + \mathbf{H}^{\text{re}}] + jk_0 Y_0 \oint_{S'} \hat{\mathbf{z}} \times \bar{\bar{\mathbf{G}}} \times \hat{\mathbf{z}} \cdot \mathbf{E}^{\text{ext}} dS' \quad (12)$$

where we have assumed that the metallic plane is at $z=0$ and hence the normal unit vectors become $\hat{\mathbf{n}} = \hat{\mathbf{n}}' = \hat{\mathbf{z}}$. If identical expansion functions are used for both the exterior surface mesh and the interior volume mesh (that is the volume shape function reduces to the surface shape function as the evaluation point approaches the surface) which results in an implicit enforcement of (10), then (12) can be substituted into (7). This results in the FE-BI equation used in Phase I

$$\int_V [(\nabla \times \mathbf{W}_i^e) \cdot \bar{\bar{\mu}}_r^{-1} \cdot (\nabla \times \mathbf{E}^{\text{int}}) - k_0^2 \mathbf{W}_i^e \cdot \bar{\bar{\epsilon}}_r \cdot \mathbf{E}^{\text{int}}] dV + k_0^2 \oint_{S'} \mathbf{W}_i^e \cdot [\hat{\mathbf{z}} \times \bar{\bar{\mathbf{G}}} \times \hat{\mathbf{z}}] \cdot \mathbf{E}^{\text{int}} = f_i^{\text{e,int}} + f_i^{\text{e,ext}} \quad (13)$$

For cavities recessed in a metallic plane, the half-space dyadic Green's function should be used in (13)

$$\bar{\bar{\mathbf{G}}} = 2\bar{\bar{\mathbf{G}}}_0 = 2 \left[\bar{\bar{\mathbf{I}}} + \frac{\nabla \nabla}{k_0^2} \right] \mathbf{G}_0 = \left[\bar{\bar{\mathbf{I}}} + \frac{\nabla \nabla}{k_0^2} \right] \frac{e^{jk_0|\mathbf{r}-\mathbf{r}'|}}{2\pi|\mathbf{r}-\mathbf{r}'|} \quad (14)$$

The FE-BI equation (13) is complete and it only remains to specify the finite elements and their associated shape functions.

B.3 Finite Element Method using Brick Elements for Anisotropic Materials

The finite element method can utilize many different finite element shapes, several of which are shown in Figure B-3.

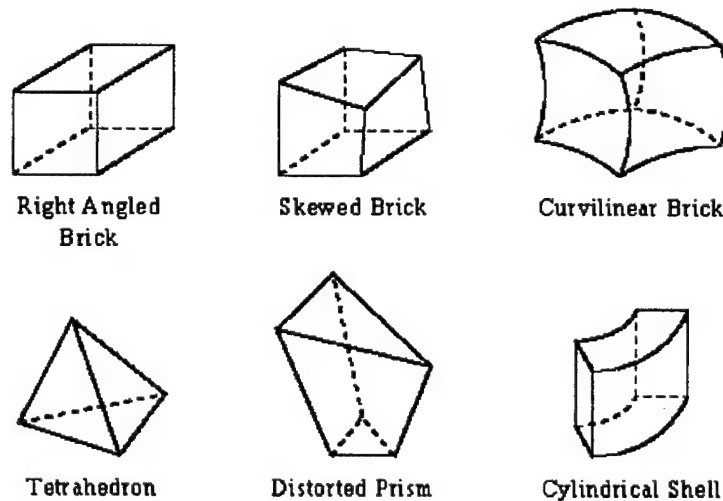


Figure B-3. Various finite element shapes.

For Phase I, both MRC and UM used brick elements such as the one shown in Figure B-4.

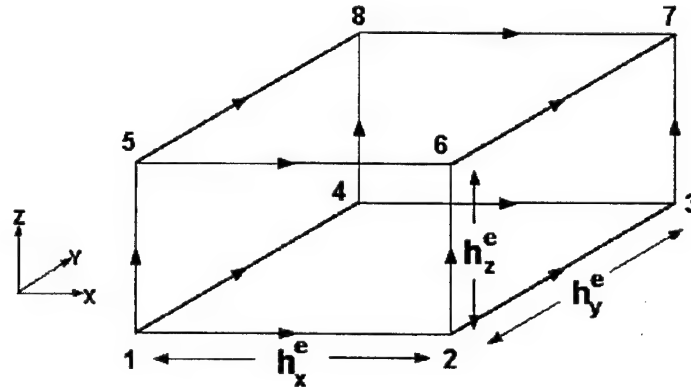


Figure B-4. Brick finite element illustrating the six nodes and twelve edges that form the brick.

These elements have two advantages:

1. the finite element volume element matrices can be solved in closed form and in fact only a small number of these interactions need be computed and stored for each layer regardless of the material variations.
2. they result in a uniform discretization of the surface aperture and this results in boundary integral matrices that are Toeplitz.

Each of these items are discussed separately.

B.3.1 Anisotropic Brick Element Matrices

The element matrices for bricks and anisotropic media can be written as

$$A^{(1)} = \int_{V_e} (\nabla \times \mathbf{W}_t^e) \cdot \bar{\bar{\mu}}_r^{-1} \cdot (\nabla \times \mathbf{W}_s^e) dV_e \quad (15)$$

$$A^{(2)} = \int_{V_e} \mathbf{W}_t^e \cdot \bar{\bar{\epsilon}}_r \cdot \mathbf{W}_s^e dV_e \quad (16)$$

where the inverse permeability and permittivity tensors are given by

$$\bar{\bar{\mu}}_r^{-1} = \begin{bmatrix} \tilde{\mu}_{xx} & \tilde{\mu}_{xy} & \tilde{\mu}_{xz} \\ \tilde{\mu}_{yx} & \tilde{\mu}_{yy} & \tilde{\mu}_{yz} \\ \tilde{\mu}_{zx} & \tilde{\mu}_{zy} & \tilde{\mu}_{zz} \end{bmatrix} \quad (17)$$

$$\bar{\bar{\epsilon}}_r = \begin{bmatrix} \epsilon_{xx} & \epsilon_{xy} & \epsilon_{xz} \\ \epsilon_{yx} & \epsilon_{yy} & \epsilon_{yz} \\ \epsilon_{zx} & \epsilon_{zy} & \epsilon_{zz} \end{bmatrix} \quad (18)$$

The interactions associated with (15) are given by

$$\begin{aligned}
 A_{xx}^{(1)} &= \frac{h_x^e h_z^e}{6h_y^e} \tilde{\mu}_{zz} \mathbf{K}_1 + \frac{h_x^e h_y^e}{6h_z^e} \tilde{\mu}_{yy} \mathbf{K}_2 + \frac{h_x^e}{4} \tilde{\mu}_{zy} \mathbf{K}_3 + \frac{h_x^e}{4} \tilde{\mu}_{yz} \mathbf{K}_3^T \\
 A_{xy}^{(1)} &= -\frac{h_z^e}{6} \tilde{\mu}_{zz} \mathbf{K}_5 + \frac{h_x^e}{4} \tilde{\mu}_{zx} \mathbf{K}_4 + \frac{h_y^e}{4} \tilde{\mu}_{yz} \mathbf{K}_6 + \frac{h_x^e h_y^e}{4h_z^e} \tilde{\mu}_{yx} \mathbf{K}_3^T \\
 A_{xz}^{(1)} &= -\frac{h_y^e}{6} \tilde{\mu}_{yy} \mathbf{K}_5^T + \frac{h_x^e h_z^e}{4h_y^e} \tilde{\mu}_{zx} \mathbf{K}_3 + \frac{h_z^e}{4} \tilde{\mu}_{zy} \mathbf{K}_6 + \frac{h_x^e}{4} \tilde{\mu}_{yx} \mathbf{K}_6 \\
 A_{yx}^{(1)} &= -\frac{h_z^e}{6} \tilde{\mu}_{zz} \mathbf{K}_5 + \frac{h_y^e}{4} \tilde{\mu}_{zy} \mathbf{K}_4 + \frac{h_x^e}{4} \tilde{\mu}_{xz} \mathbf{K}_6 + \frac{h_x^e h_y^e}{4h_z^e} \tilde{\mu}_{xy} \mathbf{K}_3^T \\
 A_{yy}^{(1)} &= \frac{h_x^e h_y^e}{6h_z^e} \tilde{\mu}_{xx} \mathbf{K}_1 + \frac{h_y^e h_z^e}{6h_x^e} \tilde{\mu}_{zz} \mathbf{K}_2 + \frac{h_y^e}{4} \tilde{\mu}_{xz} \mathbf{K}_3 + \frac{h_y^e}{4} \tilde{\mu}_{zx} \mathbf{K}_3^T \\
 A_{yz}^{(1)} &= -\frac{h_x^e}{6} \tilde{\mu}_{xx} \mathbf{K}_5 + \frac{h_y^e h_z^e}{4h_x^e} \tilde{\mu}_{zy} \mathbf{K}_3 + \frac{h_y^e}{4} \tilde{\mu}_{xy} \mathbf{K}_4 + \frac{h_z^e}{4} \tilde{\mu}_{zx} \mathbf{K}_6 \\
 A_{zx}^{(1)} &= -\frac{h_y^e}{6} \tilde{\mu}_{yy} \mathbf{K}_5^T + \frac{h_x^e h_z^e}{4h_y^e} \tilde{\mu}_{xz} \mathbf{K}_3 + \frac{h_x^e}{4} \tilde{\mu}_{xy} \mathbf{K}_4 + \frac{h_z^e}{4} \tilde{\mu}_{yz} \mathbf{K}_6 \\
 A_{zy}^{(1)} &= -\frac{h_x^e}{6} \tilde{\mu}_{xx} \mathbf{K}_5 + \frac{h_y^e h_z^e}{4h_x^e} \tilde{\mu}_{yz} \mathbf{K}_3 + \frac{h_z^e}{4} \tilde{\mu}_{xz} \mathbf{K}_4 + \frac{h_y^e}{4} \tilde{\mu}_{zy} \mathbf{K}_6 \\
 A_{zz}^{(1)} &= \frac{h_y^e h_z^e}{6h_x^e} \tilde{\mu}_{yy} \mathbf{K}_1 + \frac{h_x^e h_z^e}{6h_y^e} \tilde{\mu}_{xx} \mathbf{K}_2 + \frac{h_z^e}{4} \tilde{\mu}_{yx} \mathbf{K}_3 + \frac{h_z^e}{4} \tilde{\mu}_{xy} \mathbf{K}_3^T
 \end{aligned} \tag{19}$$

while those associated with (18) are given by

$$A^{(2)} = h_x^e h_y^e h_z^e \begin{bmatrix} \frac{\epsilon_{xx}}{36} \mathbf{K}_0 & \frac{\epsilon_{xy}}{24} \mathbf{L}_1 & \frac{\epsilon_{xz}}{24} \mathbf{L}_1^T \\ \frac{\epsilon_{yx}}{24} \mathbf{L}_1^T & \frac{\epsilon_{yy}}{36} \mathbf{K}_0 & \frac{\epsilon_{yz}}{24} \mathbf{L}_1 \\ \frac{\epsilon_{zx}}{24} \mathbf{L}_1 & \frac{\epsilon_{zy}}{24} \mathbf{L}_1 & \frac{\epsilon_{zz}}{36} \mathbf{K}_0 \end{bmatrix} \tag{20}$$

where the superscript “T” denotes a matrix transposition. The brick edge lengths, $\{h_x^e, h_y^e, h_z^e\}$ are illustrated in Figure B-4. The component matrices used in (19) and (20) are given by

$$\begin{aligned}
\mathbf{K}_0 &= \begin{bmatrix} 4 & 2 & 2 & 1 \\ 2 & 4 & 1 & 2 \\ 2 & 1 & 4 & 2 \\ 1 & 2 & 2 & 4 \end{bmatrix} & \mathbf{K}_1 &= \begin{bmatrix} 2 & -2 & 1 & -1 \\ -2 & 2 & -1 & 1 \\ 1 & -1 & 2 & -2 \\ -1 & 1 & -2 & 2 \end{bmatrix} \\
\mathbf{K}_2 &= \begin{bmatrix} 2 & 1 & -2 & -1 \\ 1 & 2 & -1 & -2 \\ -2 & -1 & 2 & 1 \\ -1 & -2 & 1 & 2 \end{bmatrix} & \mathbf{K}_3 &= \begin{bmatrix} -1 & -1 & 1 & 1 \\ 1 & 1 & -1 & -1 \\ -1 & -1 & 1 & 1 \\ 1 & 1 & -1 & -1 \end{bmatrix} \\
\mathbf{K}_4 &= \begin{bmatrix} 1 & -1 & 1 & -1 \\ -1 & 1 & -1 & 1 \\ 1 & -1 & 1 & -1 \\ -1 & 1 & -1 & 1 \end{bmatrix} & \mathbf{K}_5 &= \begin{bmatrix} 2 & 1 & -2 & 1 \\ -2 & -1 & 2 & 1 \\ 1 & 2 & -1 & -2 \\ -1 & -2 & 1 & 2 \end{bmatrix} \\
\mathbf{K}_6 &= \begin{bmatrix} 1 & 1 & -1 & -1 \\ 1 & 1 & -1 & -1 \\ -1 & -1 & 1 & 1 \\ -1 & -1 & 1 & 1 \end{bmatrix} & \mathbf{L}_1 &= \begin{bmatrix} 2 & 1 & 2 & 1 \\ 2 & 1 & 2 & 1 \\ 1 & 2 & 1 & 2 \\ 1 & 2 & 1 & 2 \end{bmatrix}
\end{aligned} \tag{21}$$

B.3.2 Boundary Integral Matrix Entries

The boundary integral in (13) can be represented as

$$I^{\text{BI}} = 2 \iint_{S'} \left[\mathbf{W}_t^e \cdot \left(\hat{\mathbf{z}} \times \overline{\overline{\mathbf{G}}_0} \times \hat{\mathbf{z}} \right) \cdot \mathbf{W}_s^e \right] dS' dS = I^{\text{BI}(1)} + I^{\text{BI}(2)} \tag{22}$$

where $\overline{\overline{\mathbf{G}}_0}$ is the free-space dyadic Green's function. From this, we recognize that

$$I^{\text{BI}(1)e} = -2 \iint_{S'} \left[\mathbf{W}_t^e \cdot \left(\hat{\mathbf{z}} \times \overline{\overline{\mathbf{G}}_0} \times \hat{\mathbf{z}} \right) \cdot \mathbf{W}_s^e \right] dS' dS \tag{23}$$

$$I^{\text{BI}(2)} = -\frac{1}{2\pi k_0^2} \iint_{S'} \left[\mathbf{W}_t^e \cdot \left(\hat{\mathbf{z}} \times \nabla \nabla \frac{e^{-jk_0 R}}{R} \times \hat{\mathbf{z}} \right) \cdot \mathbf{W}_s^e \right] dS' dS \tag{24}$$

where $R = |\mathbf{r} - \mathbf{r}'| = \sqrt{(x - x')^2 + (y - y')^2 + (z - z')^2}$. In Phase I, edge-based brick elements were used for the expansion and so these basis functions can be represented by

$$W_x^e = \frac{\tilde{s}}{h_y^e} (y - \tilde{y})$$

$$W_y^e = \frac{\tilde{s}}{h_x^e} (x - \tilde{x}) \quad (25)$$

as the evaluation point approaches the surface ($x, y, z \rightarrow 0$). In (25), the parameters \tilde{x} , \tilde{y} , and \tilde{s} are chosen based upon the particular local edge involved in the calculation. Using (25) in (23), the first class of BI interactions become

$$I_{xx}^{BI(1)} = -\frac{\tilde{s}_t \tilde{s}_s}{2\pi(h_y^e)^2} \int_{y_1^t}^{y_1^u} \int_{x_1^t}^{x_1^u} \int_{y_1^s}^{y_1^u} \int_{x_1^s}^{x_1^u} \left[(y - \tilde{y}_t)(y' - \tilde{y}_s) \frac{e^{-jk_0 R}}{R} \right] dx' dy' dx dy \quad (26)$$

$$I_{yy}^{BI(1)} = -\frac{\tilde{s}_t \tilde{s}_s}{2\pi(h_x^e)^2} \int_{y_1^t}^{y_1^u} \int_{x_1^t}^{x_1^u} \int_{y_1^s}^{y_1^u} \int_{x_1^s}^{x_1^u} \left[(x - \tilde{x}_t)(x' - \tilde{x}_s) \frac{e^{-jk_0 R}}{R} \right] dx' dy' dx dy \quad (27)$$

where the limit subscripts "l" and "u" refer to the lower and upper limits of the integration (e.g. the boundaries of the element).

The boundary integrals in (26) and (27) cannot be evaluated in closed form (as was the case with the finite element contributions given above). Rather, these integrals must be evaluated numerically and special care must be taken for the self cell (e.g. when the source and test point can coalesce). In these circumstances, the self-cell can be subdivided into sub-cells over which the basis function is assumed to be constant and closed form evaluations for the resulting sub-cell integrals

$$I^{BI(c)} = \int_{y_1^t}^{y_1^u} \int_{x_1^t}^{x_1^u} \int_{y_1^s}^{y_1^u} \int_{x_1^s}^{x_1^u} \left[\frac{e^{-jk_0 R}}{R} \right] dx' dy' dx dy \quad (28)$$

are available. For the case of interactions between different cells, simple numerical integration is sufficient.

The second boundary term requires further manipulation. Specifically, applying the divergence theorem twice and converting one of the gradient operators from ∇ to ∇' (e.g. $\nabla' G_0 = -\nabla G_0$), (24) becomes

$$I^{BI(2)} = -\frac{1}{2\pi k_0^2} \iint_{S'} \left[\nabla \cdot (\hat{z} \times \mathbf{W}_t) \nabla' \cdot (\hat{z} \times \mathbf{W}_s) \frac{e^{-jk_0 R}}{R} \right] dS' dS \quad (29)$$

Evaluating (29), using the basis function given in (25), four terms are obtained based upon the mix of test and source edge orientation

$$\begin{aligned}
I_{xx}^{BI(2)} &= -\frac{\tilde{s}_t \tilde{s}_s}{2\pi k_0^2 (h_y^e)^2} I^{BI(c)} \\
I_{xy}^{BI(2)} &= +\frac{\tilde{s}_t \tilde{s}_s}{2\pi k_0^2 (h_x^e h_y^e)} I^{BI(c)} \\
I_{yx}^{BI(2)} &= +\frac{\tilde{s}_t \tilde{s}_s}{2\pi k_0^2 (h_x^e h_y^e)} I^{BI(c)} \\
I_{yy}^{BI(2)} &= -\frac{\tilde{s}_t \tilde{s}_s}{2\pi k_0^2 (h_x^e)^2} I^{BI(c)}
\end{aligned} \tag{30}$$

Once again, the $I^{BI(c)}$ terms in (30) must be evaluated by subdivision and closed form expressions for the self-cell, and via numerical integration for the remainder of the interactions.

C. Ferrite Material Model

The FE-BI formulation presented in Section B is valid for arbitrary anisotropic materials. The focus of this SBIR project on the other hand is a anisotropic material with special properties, ferrites. These material exhibit dispersive properties that can be manipulated by adjusting the strength and orientation of a static magnetic field. That is the material “looks” different to a dynamic field as the static “control” field is altered. In this section, the ferrite material model will be presented along with some important parameters and terms that will be used throughout this report.

The most common representation of the material properties of a ferrite involve a scalar permittivity (typically fairly large ~9 to 16) and a tensor permeability with different forms depending on the orientation of the applied static bias field (e.g. this field is polarized along the direction of the length of the magnet). The Pölder tensor for the three Cartesian directions are given by

$$\begin{aligned}
\bar{\bar{\mu}}_r &= \begin{bmatrix} 1 & 0 & 0 \\ 0 & \mu & j\kappa \\ 0 & -j\kappa & \mu \end{bmatrix} \quad \text{x-bias} \\
\bar{\bar{\mu}}_r &= \begin{bmatrix} \mu & 0 & j\kappa \\ 0 & 1 & 0 \\ -j\kappa & 0 & \mu \end{bmatrix} \quad \text{y-bias} \\
\bar{\bar{\mu}}_r &= \begin{bmatrix} \mu & j\kappa & 0 \\ -j\kappa & \mu & 0 \\ 0 & 0 & 1 \end{bmatrix} \quad \text{z-bias}
\end{aligned} \tag{31}$$

where the μ and κ terms are given by

$$\mu = \left(1 + \frac{\omega_0 \omega_m}{\omega_0^2 - \omega^2} \right) = \left(1 + \frac{f_0 f_m}{f_0^2 - f^2} \right) \quad (32)$$

$$\kappa = \left(\frac{\omega \omega_m}{\omega_0^2 - \omega^2} \right) = \left(\frac{f f_m}{f_0^2 - f^2} \right) \quad (33)$$

and $\omega = 2\pi f$. The Pölder tensors (31) are given assuming the “engineer’s time convention” of $e^{+j\omega t}$. The corresponding tensors for the “physicist’s” time convention are obtained by taking the complex conjugate of (31).

In (32) and (33), several different important frequencies are used. The operating frequency is denoted by f . The Lamor or precession frequency is indicated by f_0 while the forced precession frequency is represented by f_m . The precession frequency in MHz is given by

$$f_0^{\text{MHz}} = 2.8 \times H_0 \quad (34)$$

where H_0 is the applied static magnetic bias field *within the ferrite sample* and in (34) this quantity is assumed to be given in terms of Oersteds (Oe). Note that H_0 is not necessarily equal to the external applied static magnetic field (H_e) since for practical sample geometries, demagnetization may occur such that $H_0 \leq H_e$ depending on sample geometry and applied field orientation. The interested reader is encourage to review Pozar’s text book chapter concerning ferrite materials for further details¹. The forced precession frequency in MHz is given by

$$f_m^{\text{MHz}} = 2.8 \times (4\pi M_s) \quad (35)$$

where the saturation magnetization ($4\pi M_s$) is assumed to be given in Gauss. M_s is the peak magnetization achieved within a ferrite sample as an increasingly strong static bias field is applied. Hence it represents an important intrinsic material property of ferrites.

The co-pol permeability represented by (32) and (33) includes no magnetic loss. To include such loss, a line width is typically used. This line width (ΔH) is illustrated in Figure C-1

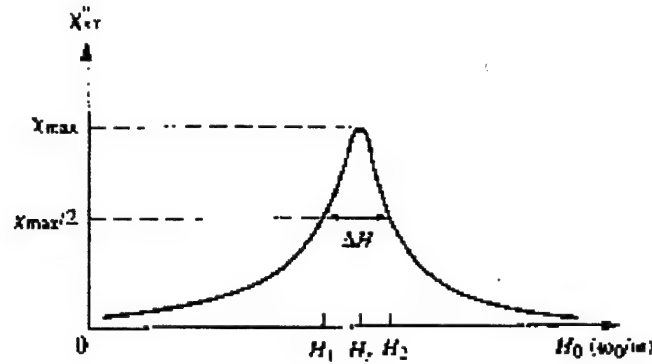


Figure C-1. Illustration of magnetic line width (After Pozar[1]).

and the effect is to modify (34) by including in an imaginary component

$$f_0^{\text{MHz}} = 2.8 \times \left(H_0 + j \frac{\Delta H}{2} \right) \quad (36)$$

Hence, the forced precession frequency is now complex rather than purely real.

An important parameter for total electric field finite element analysis, such as the formulation presented in Section B is the inverse permeability tensor

$$\begin{aligned} \bar{\bar{\mu}}_r^{-1} &= \begin{bmatrix} 1 & 0 & 0 \\ 0 & \mu/\Delta & -j\kappa/\Delta \\ 0 & +j\kappa/\Delta & \mu/\Delta \end{bmatrix} & \text{x-bias} \\ \bar{\bar{\mu}}_r^{-1} &= \begin{bmatrix} \mu/\Delta & 0 & -j\kappa/\Delta \\ 0 & 1 & 0 \\ +j\kappa/\Delta & 0 & \mu/\Delta \end{bmatrix} & \text{y-bias} \\ \bar{\bar{\mu}}_r^{-1} &= \begin{bmatrix} \mu/\Delta & -j\kappa/\Delta & 0 \\ +j\kappa/\Delta & \mu/\Delta & 0 \\ 0 & 0 & 1 \end{bmatrix} & \text{z-bias} \end{aligned} \quad (37)$$

where the determinant of the tensor (31) is given by $\Delta = \mu^2 - \kappa^2$.

Several interesting phenomena and/or difficulties arise as a result of the various frequency parameters associated with a ferrite material (e.g. f_0 , f_m , H_0 , ΔH , and $4\pi M_s$). For example, when the operating frequency is equal to the precession frequency $f = f_0$, a gyromagnetic resonance occurs and the

ferrite permeability is infinite. Since the skin depth is inversely proportional to the permeability, at the gyromagnetic resonance, the field cannot penetrate into the ferrite sample. Alternatively, the ferrite sample is very lossy. This condition cannot occur when a magnetic loss is included since the forced precession frequency is complex while the operating frequency is real. Another interesting phenomena occurs when the effective permeability (See Section E) becomes zero. At this frequency, a anti-ferromagnetic resonance (AFMR) occurs and the skin depth is infinite. Hence, the ferrite is perfectly transparent. These are narrow band effects, however, there is some hope for extending these effects over a wider bandwidth and this is will be the subject of future research.

A difficulty in the total electric field finite element formulation occurs when the precession frequency is real. At some frequency, the determinant vanishes (e.g. when $|\mu| = |\kappa|$) and hence the inverse tensor (37) does not exist. Once again, inclusion of a small magnetic loss ($\Delta H \neq 0$) will avoid this problem. In addition, as UM has discovered, the material model presented above leads to solution difficulties at certain frequencies and UM's findings will be discussed in greater detail in a following section.

Ferrite materials, due to their Hermetian (complex conjugate, transposed) tensor structure, exhibit several interesting features. The polarization properties depend on the orientation of the applied bias field as shown in (31) and (37). For example, for a z-biased condition, ferrite materials "look" different to right-hand circular and left-hand circular polarized fields. Hence, the propagation velocity, loss, and other physical effects are different. This property suggests various special uses for ferrites in antenna design. Alternatively, depending on the bias state, a ferrite material can look nearly transparent to one polarization and nearly opaque to the orthogonal polarization.

D. Validation

Both MRC and UM modified their respective FE-BI brick computer programs to accommodate anisotropic, and in particular ferrite, materials. Both organizations did these modifications in parallel to assure transfer of information between MRC and UM and to provide both organizations with a first-hand understanding of the issues involved in writing FE-BI computer programs for ferrites. This is an important "learning curve" opportunity for both MRC and UM since in Phase II, both organizations are tasked with computer program development that will eventually be merged into one common program.

The specific modifications to each organization's software were:

1. Implementing the anisotropic finite element matrices given in Section B (note, the isotropic material matrices are obtained by setting all diagonal terms of the permittivity and permeability tensors to identical, non-zero numbers, and setting all other tensor entries to zero).
2. Implementing an asymmetric iterative matrix solver.
3. Automatic calculation of the permeability tensor for ferrites given the appropriate parameters.

MRC implemented a biconjugate gradient (BiCG), conjugate gradient squared (CGS), and biconjugate gradient stabilized (BiCG-STAB) iterative matrix solvers. The BiCG method was found to be the preferred algorithm in terms of convergence rate and ability to reach a converged condition. The solution generated using the BiCG algorithm and a LU decomposition solver (LINPACK) is shown in Figure D-1.

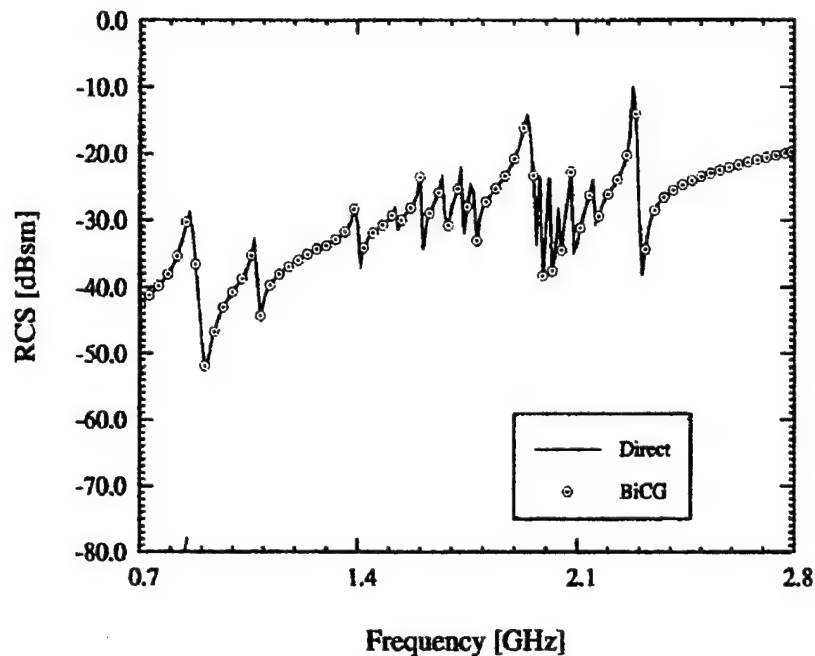


Figure D-1. Agreement between BiCG and LU decomposition solvers.

Although this particular geometry exhibited solution difficulties near the forced precession frequency (2.4 GHz for this example), the agreement between the BiCG and LU decomposition solvers demonstrates the validity of the BiCG solver as implemented by MRC for asymmetric matrices.

The next validation task was to compare MRC's and UM's computer programs with published reference data. This was a difficult task for two reasons:

1. The published data rarely corresponded to a cavity-backed geometry (which is what the FE-BI computer program assumed) and hence any comparisons involved potentially important geometrical approximations.
2. Published solutions often were not consistent with one another, likely due to the special difficulties in modeling ferrite material.

Various sources were used and the comparisons along with a brief discussion of each will be presented in turn.

D.1 Cavity-backed Apertures

One source of reference data that was particularly useful was found in Dr. David Kokotoff's Ph.D. dissertation². In this work, Dr. Kokotoff developed a method of moments (MoM) computer program for cavity-backed, ferrite loaded apertures. This is essentially the MoM equivalent of MRC's FE-BI computer program, except the MoM program is only capable of modeling layered cavity fills as opposed to fully inhomogeneous fills. Nevertheless, the data published in [2] was useful for comparison. Figure D-2 illustrates a geometry used by both Kokotoff and MRC.

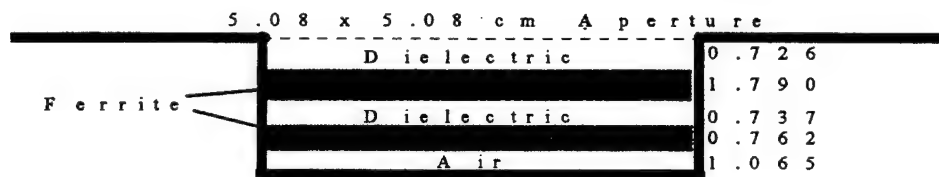


Figure D-2. Layered cavity-backed aperture used for comparison between MoM and FE-BI.

Kokotoff ran his MoM computer program for various bias states ($400 \text{ Oe} \leq H_0 \leq 700 \text{ Oe}$) and recorded the radar cross section (RCS) within a 300 MHz bandwidth. His results are reproduced in Figure D-3.

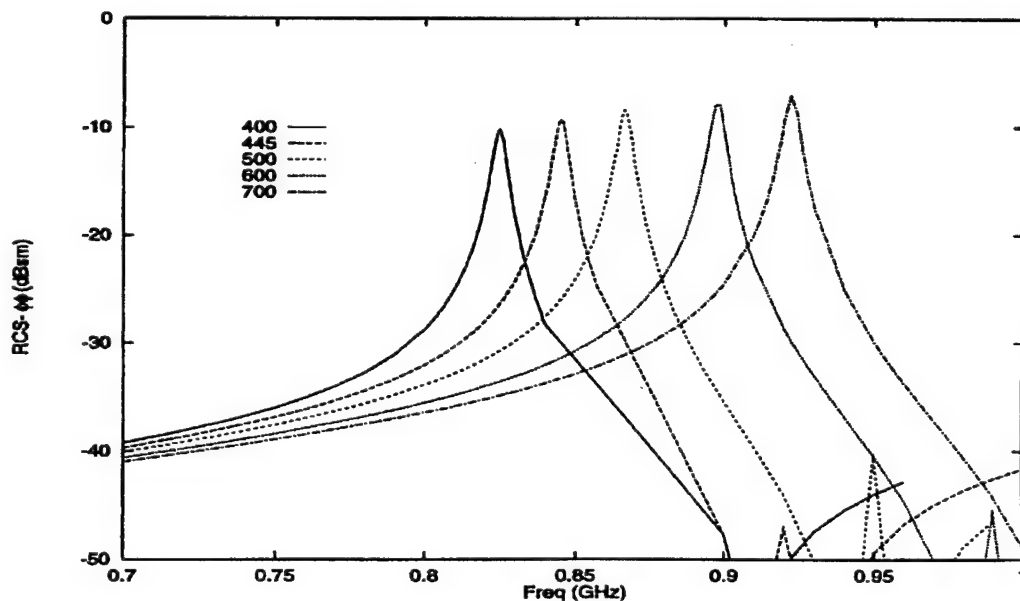


Figure D-3. Reproduction of Figure 6.1 in [2].

MRC's results for the same geometry (see Figure D-2) are presented in Figure D-4.

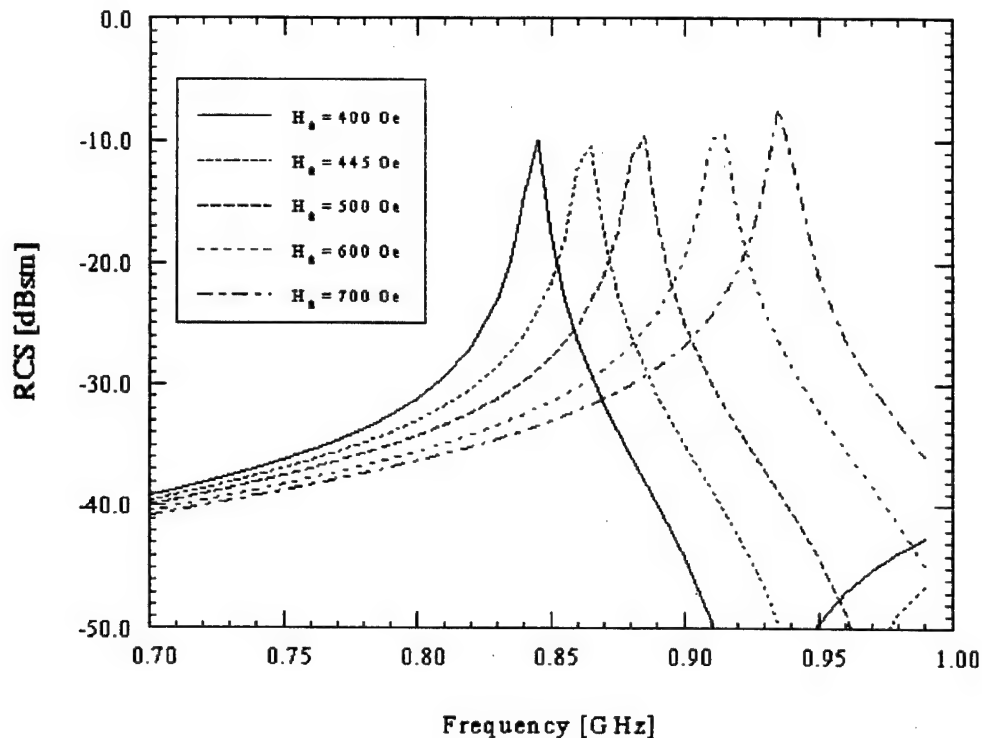


Figure D-4. MRC's FE-BI comparison to Figure D-3.

The agreement is quite good. This result is significant in that it demonstrates the validity of the FE-BI implementation by comparison with a totally different formulation.

Not all comparisons between Kokotoff's results and either MRC's or UM's results were favorable. Tremendous difficulty was encountered for certain frequency ranges and both MRC and UM conclude that in these bands, the ferrite material exhibits behavior that is ill-favorable for electric field FE-BI analysis. For example, in the vicinity of the forced precession frequency (and an unbiased ferrite sample) as mentioned previously, the determinant of the permeability tensor goes to zero and hence the inverse permeability tensor is not defined. This results in erratic behavior and ill-conditioned matrices. Figure D-5 illustrates the condition number for a dielectric- and ferrite-filled cavity problem. In this, the dielectric (isotropic) condition number is generally good and even its peak near 2.2 GHz is not too bad. However, clearly the ferrite-filled case exhibits poor conditioning just below the aperture resonance (~ 2.2 GHz) and near the forced precession frequency (~ 2.4 GHz). For this case, the bias field was shut off and no magnetic loss was assumed, so the determinant of the permeability tensor vanished at 2.4 GHz.

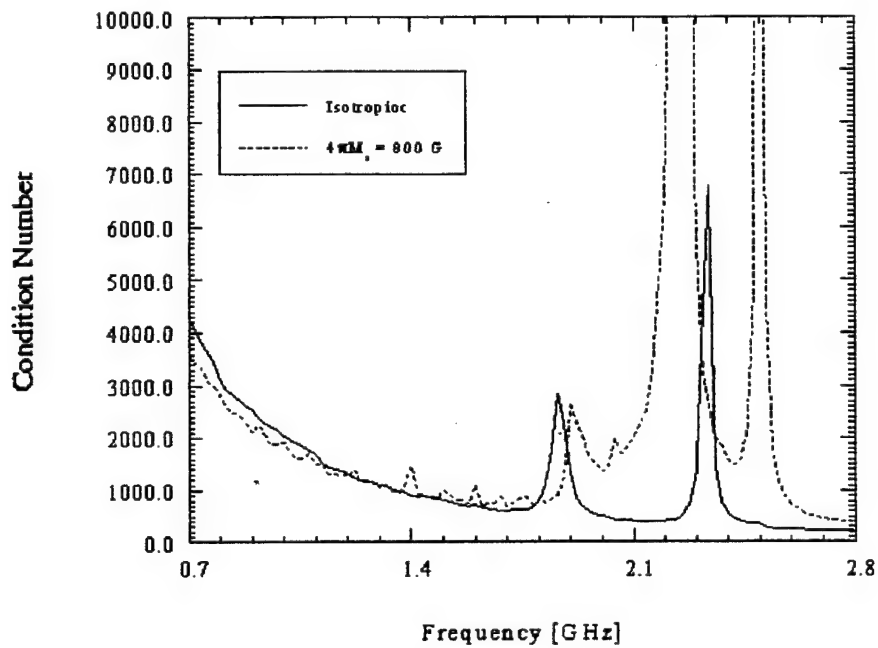


Figure D-5. Condition number verses frequency (large condition numbers indicate a poorly conditioned matrix).

D.2 Patch Antennas

Patch antennas are another class of antennas investigated under this effort. Unfortunately, the available reference data for ferrite-backed patch antennas assume an infinite ferrite substrate whereas the FE-BI computer program used by MRC and UM assume a finite cavity below the patch. Figure D-6 reproduces a RCS calculation for a ferrite-backed patch antenna presented by Pozar³.

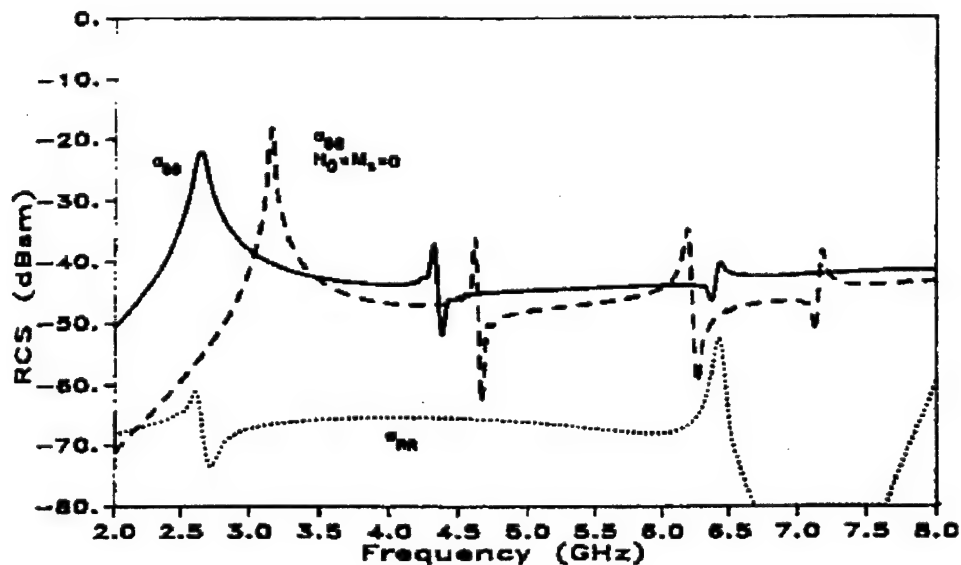


Figure D-6. Reproduction of Pozar's [3] results.

Figure D-7 illustrates MRC's results for the same patch antenna (except the substrate is recessed in a cavity rather than being an infinite grounded ferrite slab).

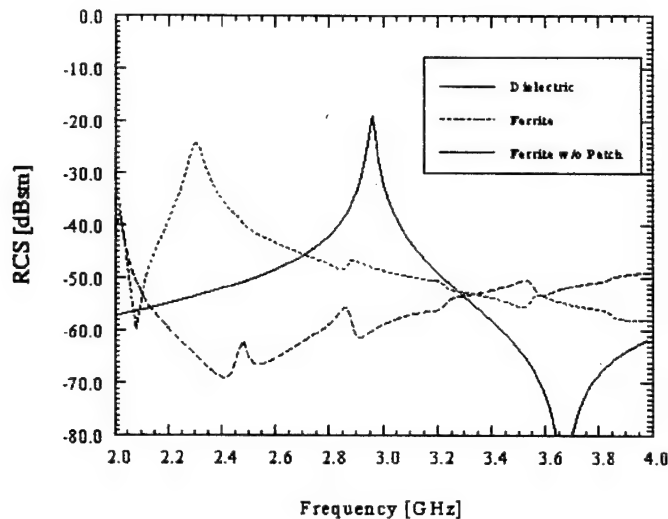


Figure D-7. Scattering by a 1.3x1.3 cm patch antenna recessed in a 2.6x2.6x0.13 cm ferrite filled cavity.

The agreement is good except for low frequencies where the cavity-backed structure is not a good approximation to the original grounded ferrite slab. This is due to the fact that below resonance, aperture edges are not electrically far from the patch and hence their presence has a greater effect on the scattered fields attributed to the patch antenna.

E. Convergence Issues

Several factors affect the convergence properties of iterative matrix solvers. These include:

1. Aspect ratio of elements (e.g. large differences in element shapes throughout the mesh is bad).
2. Excitation (typically radiation analysis requires more iterations than RCS analysis).
3. Formulation (FE-BI is generally better conditioned than FE-ABC, FE-AA, or FE-PML).
4. Material properties (anisotropic is often more difficult to solve than isotropic materials).

This section concentrates on the last item since it is particular to ferrite materials[†].

E.1 Propagation Constants

Although convergence was achieved for the previous examples, convergence difficulties were encountered while studying the ferrite materials. To examine the reason behind these convergence difficulties, it is necessary to look at the wave modes which are excited within the ferrite region. These modes are linked to the propagation constants within the ferrite material. A correlation can be made between the propagation constants and the regions of non-convergence.

[†] This section is taken verbatim from a report submitted by UM to MRC in April 1997.

When dealing with ferrite materials, the field behavior is determined by the propagation direction and its orientation with the applied magnetic bias field direction. There are two separate cases which determine the effective permeability (μ_{eff}) within the ferrite - the longitudinal case where the propagation is parallel to the applied bias field and the transverse case where propagation is perpendicular to the applied bias field. In the longitudinal case

$$\mu_{\text{eff}} = \mu \pm \kappa \quad (38)$$

whereas in the transverse case

$$\mu_{\text{eff}} = \frac{\mu^2 - \kappa^2}{\mu} \quad (39)$$

For both instances, the propagation constant within the ferrite is calculated as

$$\gamma = j\omega\sqrt{\epsilon_0\mu_0\epsilon_r\mu_{\text{eff}}} = jk_0\sqrt{\epsilon_r\mu_{\text{eff}}} = \alpha + j\beta \quad (40)$$

A careful study of the solver convergence rate for various propagation constants was done. It provided the conclusion that convergence behavior can be predicted, by looking at each of the ferrite modes and the associated μ and κ parameters.

E.1.1 Ferrite Cavity Example

To demonstrate the correlation between γ and convergence, the geometry shown in Figure E-1 was considered.

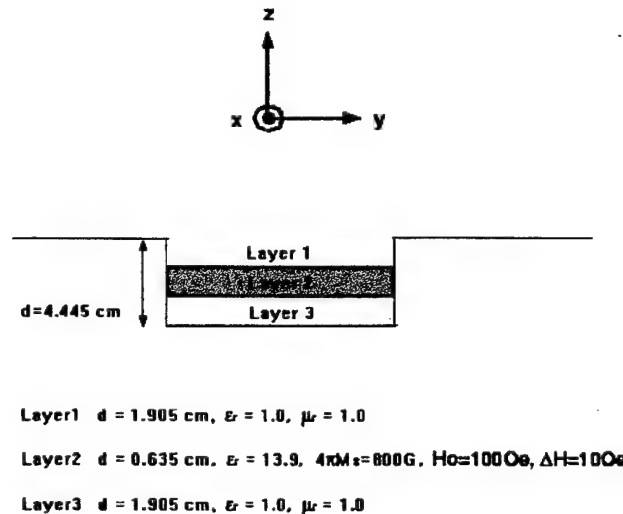


Figure E-1. Ferrite cavity geometry.

In this example, $H_0 = 100$ Oe and Figure E-2 and Figure E-3 show the behavior of μ and κ , respectively, verses frequency.

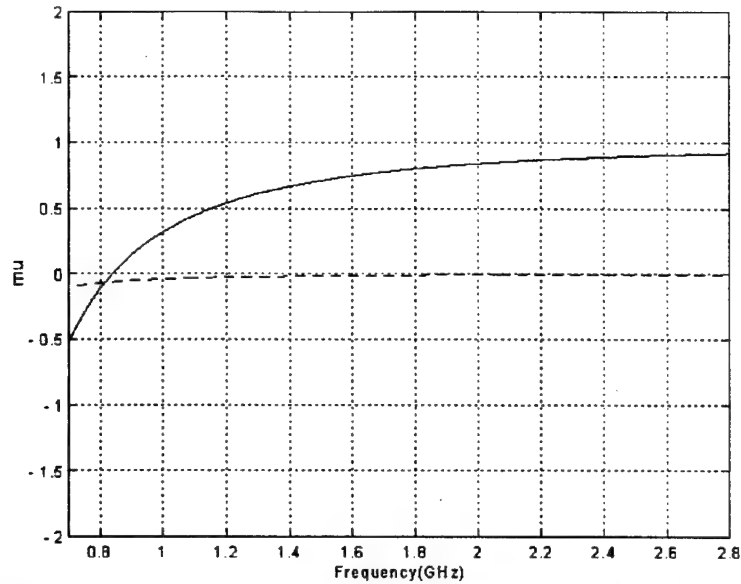


Figure E-2. μ vs. f , $H_0 = 100 \text{ Oe}$, $4\pi M_s = 800 \text{ G}$, $\Delta H = 10 \text{ Oe}$.

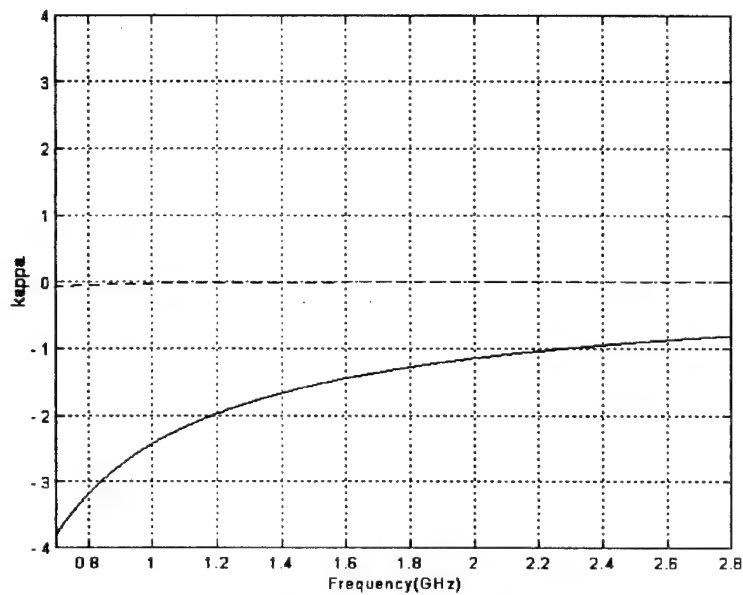


Figure E-3. κ vs. f , $H_0 = 100 \text{ Oe}$, $4\pi M_s = 800 \text{ G}$, $\Delta H = 10 \text{ Oe}$.

We observe that μ is less than unity for all frequencies in the desired range, and this situation is similar to the dual case of ϵ_r less than one. The latter is associated with plasma behavior of the ionosphere. At those frequencies where ϵ_r is less than one, the ionosphere becomes completely reflective and gives rise to the phenomenon of short wave propagation around the earth.

Figure E-4 and Figure E-5 show α and β for three different values of μ_{eff} . Excluding the mode with $\mu_{\text{eff}} = \mu - \kappa$, the other two modes have β nearly zero for all frequencies. More specifically β exhibits a filter-like behavior from 1.3 - 2.5 GHz as demonstrated in Figure E-5 for the extraordinary

(transverse) mode. Interestingly, the convergence curve in Figure E-6 shows that the convergence is very slow or not achieved in the band where $\beta \approx 0$.

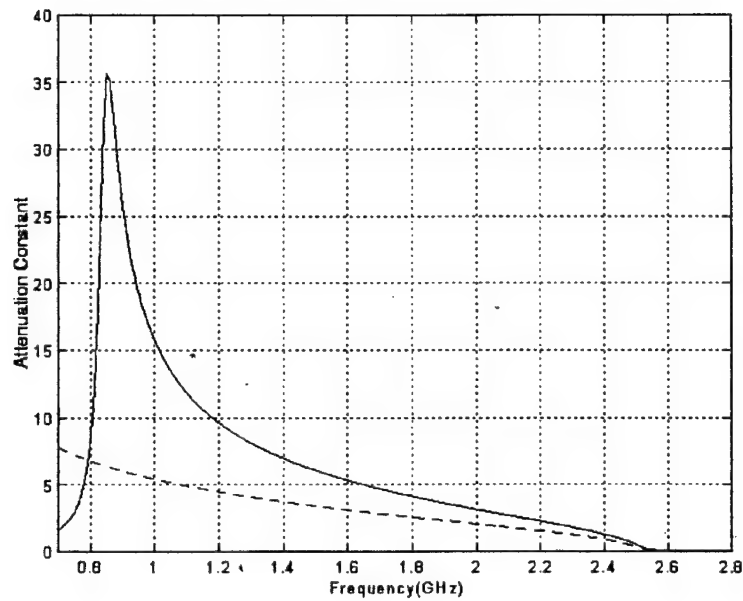


Figure E-4. α normalized to k_0 , $-\mu_{\text{eff}} = \frac{\mu^2 - \kappa^2}{\mu}$, $--\mu_{\text{eff}} = \mu + \kappa$, $-\cdot-\mu_{\text{eff}} = \mu - \kappa$

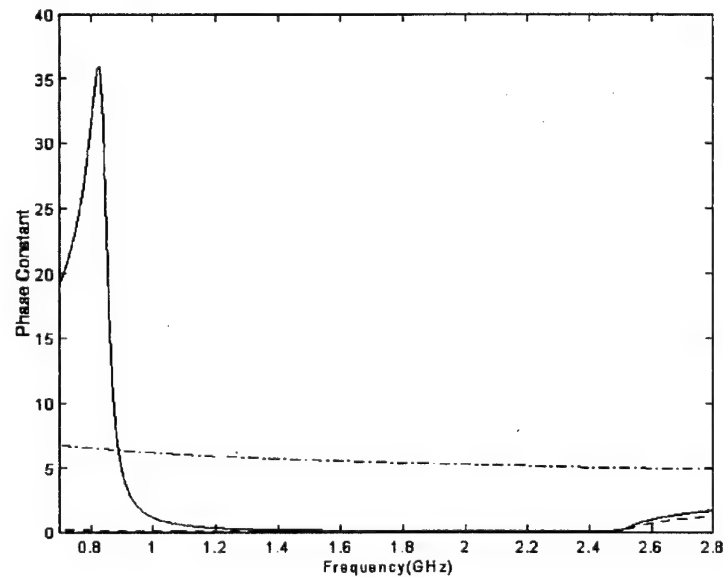


Figure E-5. β normalized to k_0 , $-\mu_{\text{eff}} = \frac{\mu^2 - \kappa^2}{\mu}$, $--\mu_{\text{eff}} = \mu + \kappa$, $-\cdot-\mu_{\text{eff}} = \mu - \kappa$

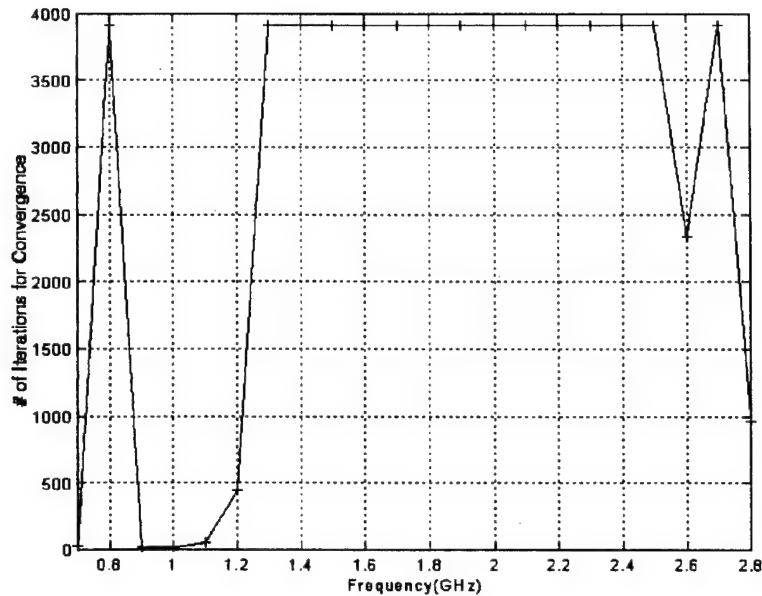


Figure E-6. Convergence performance, $H_0 = 100 \text{ Oe}$, # of unknowns = 3915.

E.1.2 Ferrite Cavity with Patch Antenna Example

Figure E-7 and Figure E-8 show the frequency behavior of μ and κ . From the figures, both μ and κ can have negative values for the frequency range considered. Also Figure E-9 and Figure E-10 show that the attenuation and phase constants exhibit a behavior similar to the ferrite cavity. Once again, the convergence performance (See Figure E-11) is governed by the behavior of the transverse β . When β is nearly zero, we again see that no convergence is achieved. More specifically, the frequencies at which the transverse β is zero corresponds to the frequency band of non-convergence.

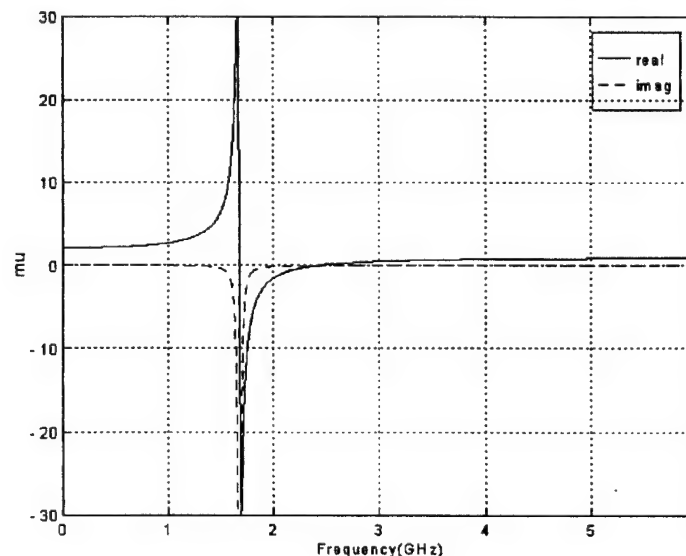


Figure E-7. μ vs. f , $H_0 = 600 \text{ Oe}$, $4\pi M_s = 650 \text{ G}$, $\Delta H = 30 \text{ Oe}$.

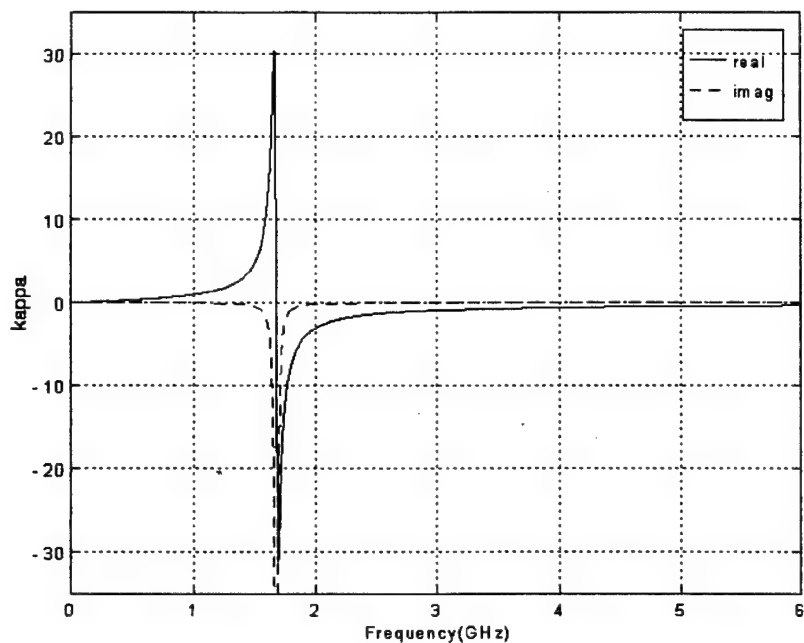


Figure E-8. κ vs. f , $H_0 = 600 \text{ Oe}$, $4\pi M_s = 650 \text{ G}$, $\Delta H = 30 \text{ Oe}$.

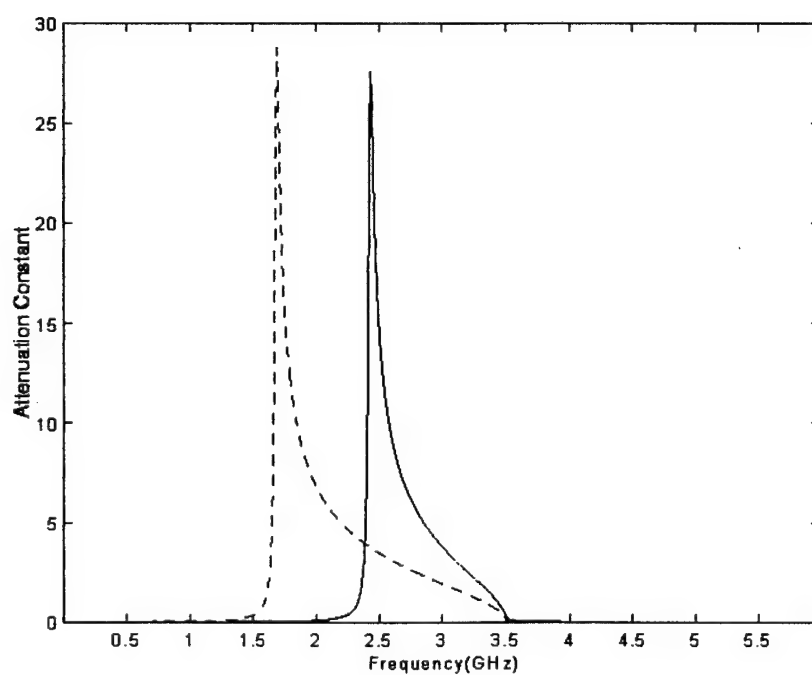


Figure E-9. α normalized to k_0 , $-\mu_{\text{eff}} = \frac{\mu^2 - \kappa^2}{\mu}$, $-\mu_{\text{eff}} = \mu + \kappa$, $-\mu_{\text{eff}} = \mu - \kappa$

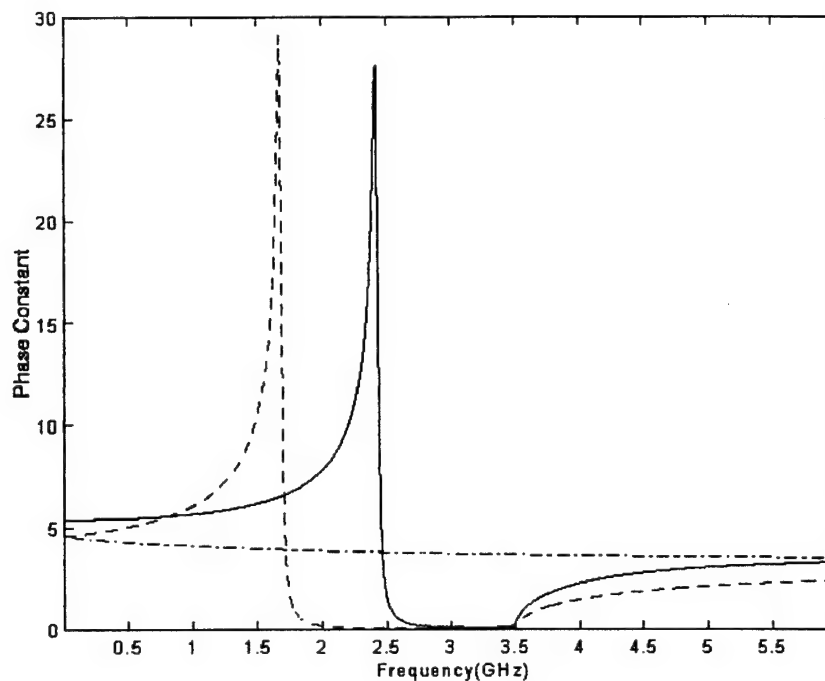


Figure E-10. β normalized to k_0 , $-\mu_{\text{eff}} = \frac{\mu^2 - \kappa^2}{\mu}$, $--\mu_{\text{eff}} = \mu + \kappa$, $- \cdot \mu_{\text{eff}} = \mu - \kappa$

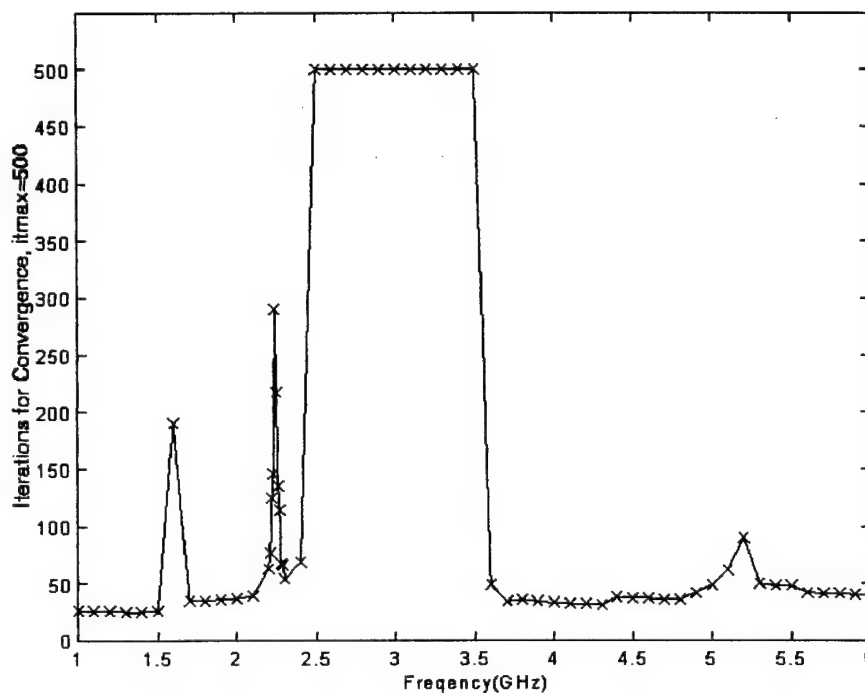


Figure E-11. Convergence performance, $H_0 = 100$ Oe, # of unknowns = 3766.

F. Phase I Trade Studies

MRC and UM conducted a number of trade studies during Phase I to establish the feasibility of applying finite element analysis to ferrite materials and to aid in the definition of a Phase II development plan. This section presents the results of these trade studies.

F.1 Perfectly Match Layer Mesh Truncation

The University of Michigan has been studying the use of perfectly matched layer (PML) mesh truncation condition. Their work has involved the anisotropic PML formulation first presented by Sacks, et al.⁴. Figure F-1 illustrates this anisotropic PML. Use of this PML on curved boundaries has not been established and therefore was investigated by UM. In addition, since this PML has various parameters, a trade study to determine the optimal parameter mix was undertaken. Figure F-2 illustrates the results of this trade study. From this chart, an absorber designer can determine the optimal parameters which result in a minimally thick absorber with maximum absorption for a given number of absorber layers.

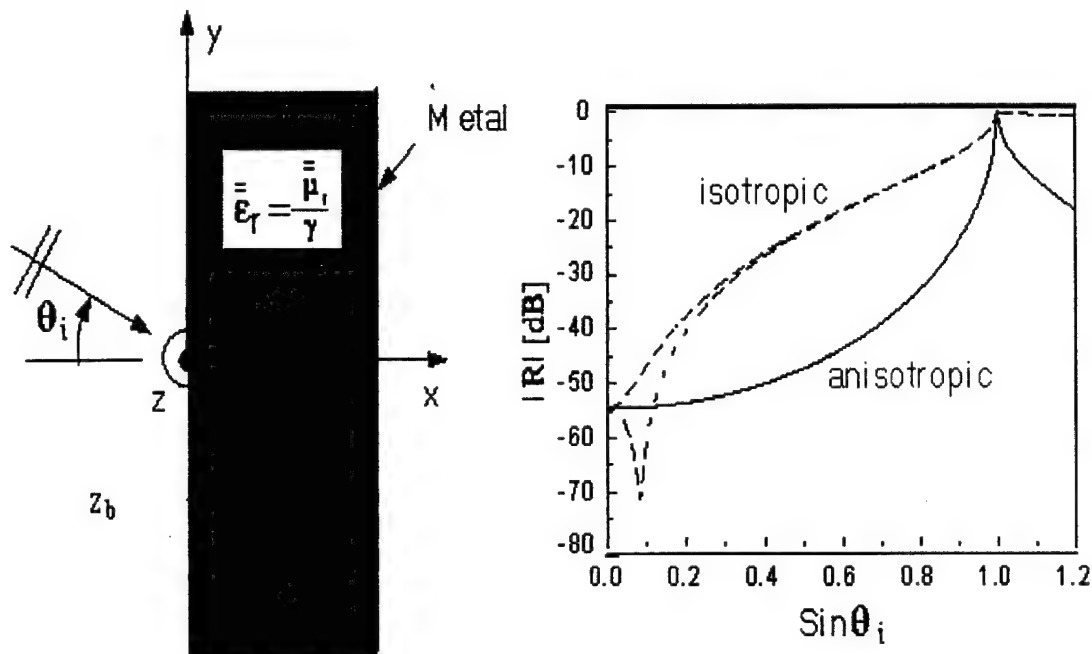


Figure F-1. Comparison of new anisotropic PML and traditional PML.

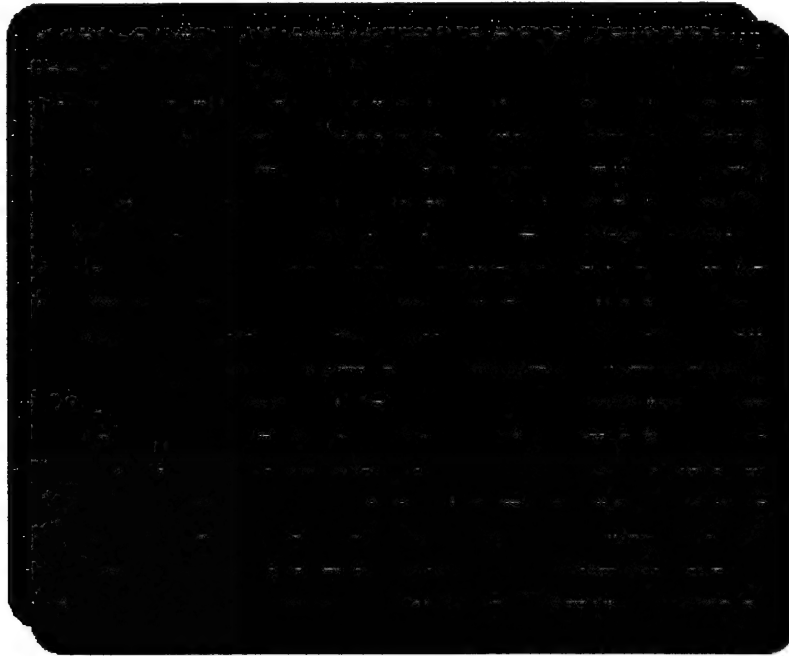


Figure F-2. PML absorber design curves where $\beta t/\lambda_0$ is the thickness of the PML and N is a PML parameter describing the material properties. The straight lines give $|R|$ in dB and the curved lines give N : (—) exact $|R|$, (···) homogeneous case and (— · — ·) inhomogeneous case.

F.1.1 Curved PML Trade Study

UM undertook a trade study to determine the performance of the PML for curved surfaces. Their overall conclusion is that this PML will work well for a curved surface; however, not as well as in the case of a flat surface. This PML is superior to more traditional second order absorbing boundary conditions (ABCs). Figure F-3 illustrates UM's results.

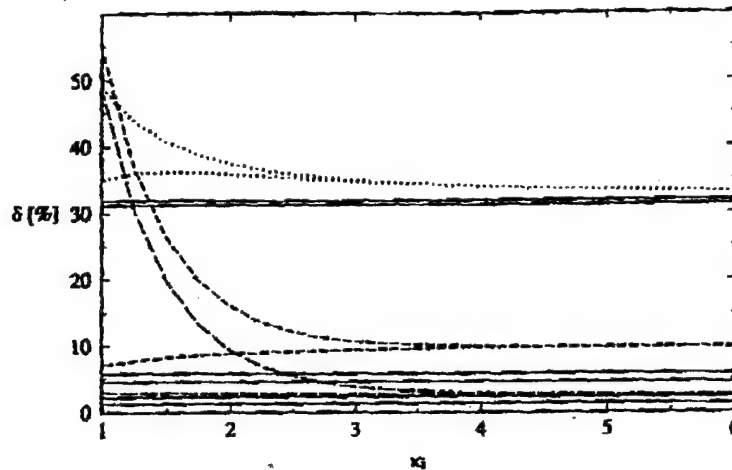


Figure 6: δ for ABCs and material absorbers with $x_0 = 10$, $d = \lambda_0/2$ and $\kappa = 1 - j\kappa_i$: (—) ABCs, (.....) homogeneous isotropic material, (- - -) homogeneous anisotropic material and (- · -) inhomogeneous anisotropic material. For the materials, the top curve is for a layer with $\tau = 0.18\lambda_0$ and the bottom one is for an infinite medium.

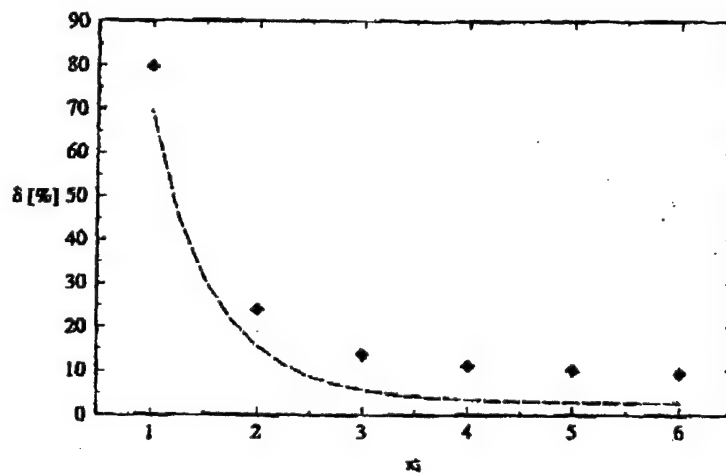


Figure 7: δ for analytical and FEM results with $x_0 = 10$, $d = \lambda_0/2$, $\tau = 0.15\lambda_0$ and $\kappa = 1 - j\kappa_i$: (—) analytical and (♦ ♦ ♦) FEM.

Figure F-3. Results of the curved PML trade study.

F.2 Matrix Iterative Solvers and Conditioning

UM undertook a study of various iterative matrix solvers due to MRC's preliminary discovery that ferrite materials have a rather detrimental effect on the matrix condition number. UM found that the GMRES solver required fewer iteration than either the BiCG or QMR algorithms (this is to be expected based upon published results in the literature). Figure F-4 illustrates the convergence behavior of these three iterative solvers (QMR, BiCG, and GMRES) for a 3000 unknown problem.

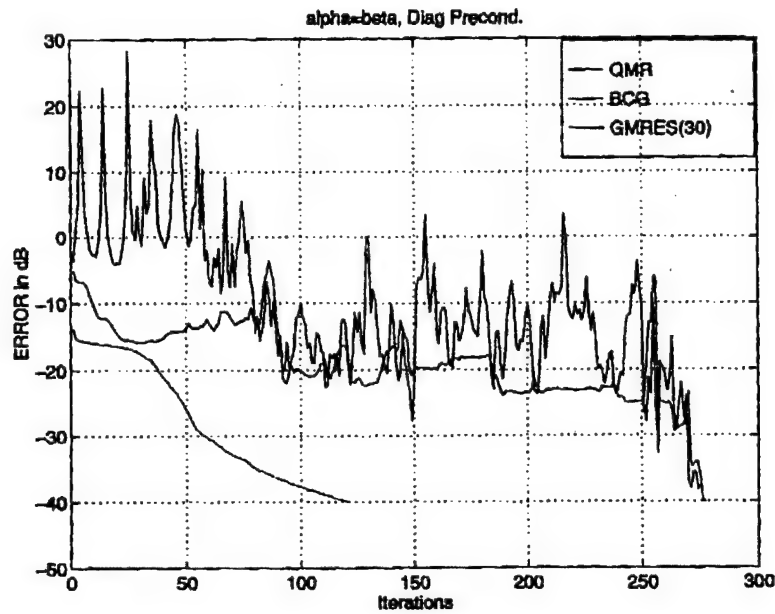


Figure F-4. Convergence behavior for three iterative solvers (3000 unknowns).

A study of the benefits of using matrix preconditioning was also undertaken. Figure F-5 illustrates the benefits of such preconditioning. Preliminary indication from both MRC and UM research staff indicates that preconditioning is essential to achieving reliable and accurate result from a finite element analysis when ferrite materials are present.

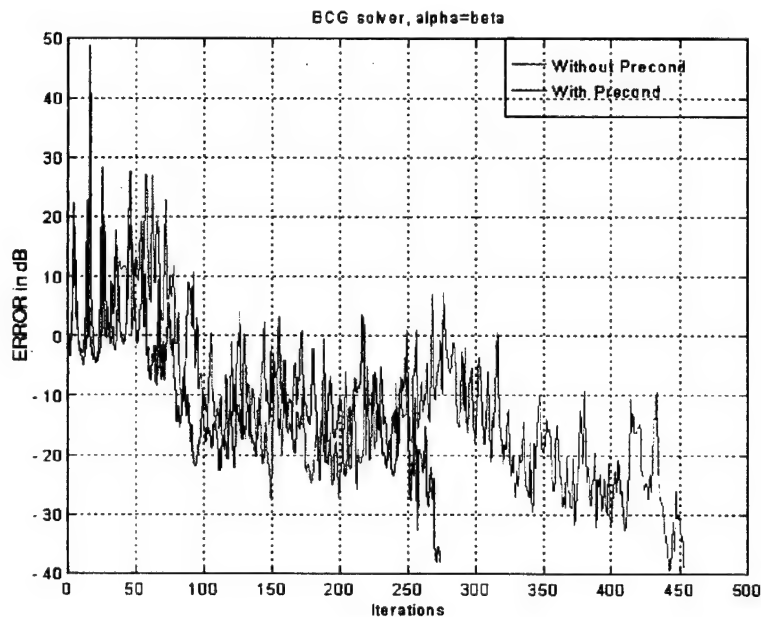
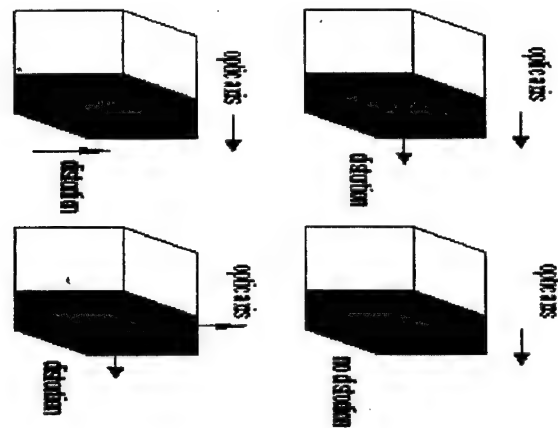


Figure F-5. Convergence behavior of an iterative solution with and without preconditioning.

F.3 Element Distortion

UM also investigated the effect of element distortion on condition number. It is a well known fact that the best conditioned matrices result from elements that have roughly a 1:1:1 aspect ratio. That is, all edges of the element are approximately equal. Often it is not possible to obtain such elements without a high computational cost in terms of number of unknowns (e.g. lots of small elements). Distortion of the elements is expected to be especially important for ferrite materials due to their anisotropic permeability. Figure F-6 illustrates the cases investigated by UM and Figure F-7 presents UM's results.



Terminology:

- *No distortion*: the block size is $a \times b \times c$ (original)
- *Distortion*: along y (say), if the block size becomes $a \times B \times c$ where distortion (in logarithm) $\log_{10} \frac{B}{b}$.
- *Condition number*: if A is a system matrix, then condition number may be determined by: $\|A\|_p \|A^{-1}\|_p$.
- *Normalized cond. number*: normalized to that of non-distorted system.

Figure F-6. Element distortion cases examined (data shown in Figure F-7).

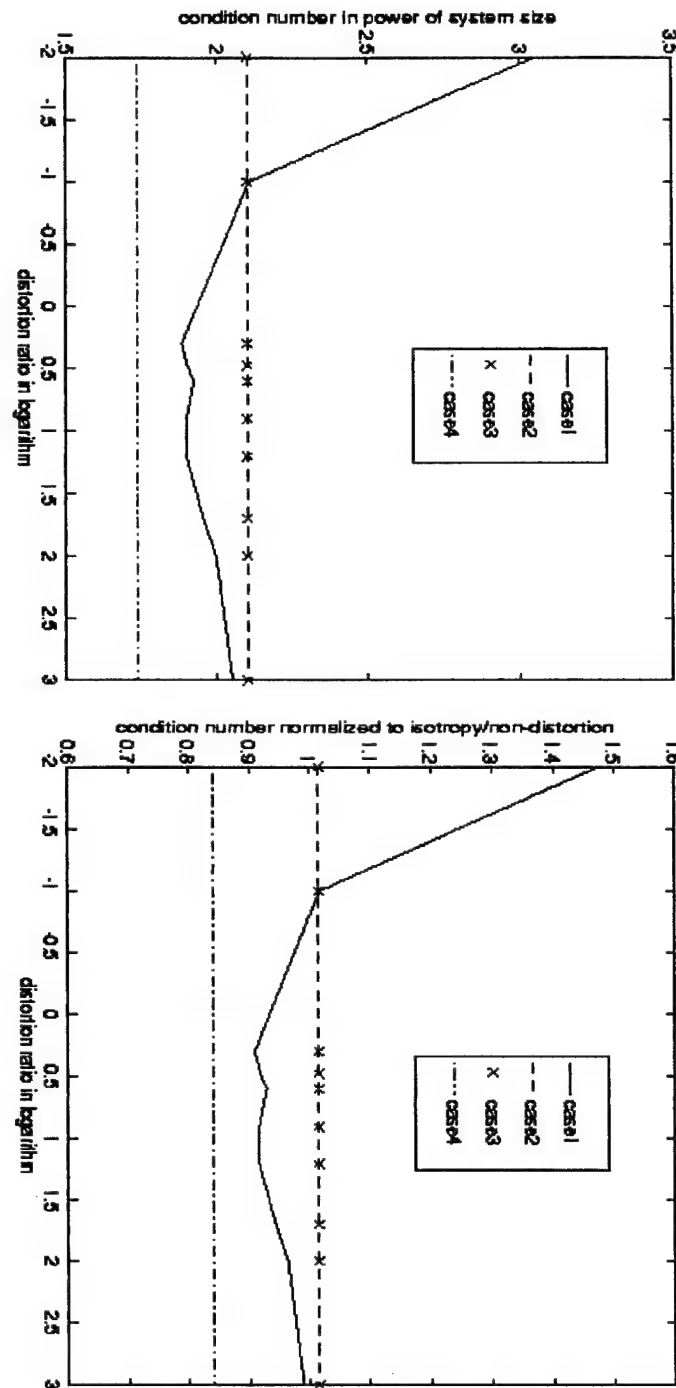


Figure F-7. Effect of element distortion on matrix condition number. The cases correspond to the four brick images shown in Figure F-6.

G. Ferrite-backed Patch Antenna Examples

MRC and UM exercised the FE-BI computer programs developed during Phase I to investigate the radiation properties of ferrite-backed antennas. This section presents a sample of our results.

G.1 Radiation Properties of a Single Ferrite-backed Patch Antenna

As a partial attempt to answer the question, "What good are these antennas?", MRC has investigated the radiation properties of a particular patch antenna using our FE-BI computer program, LM_BRICK. The antenna chosen for initial study was the one used by Prof. Pozar to demonstrate polarization diversity [3]. This antenna was 0.61 x 0.61 cm printed on a 0.127 cm thick ferrite substrate. The substrate had a dielectric constant of 15 and a magnetization saturation of 650 Gauss. The substrate was normally (z-axis) biased.

For our study, we placed the antenna cited above in a 1.22 x 1.22 cm metallic cavity and considered the transverse (x- and y-axis) as well as normally biased (z-axis) cases. Pozar's integral equation formulation allowed investigation of only the normally biased case. We found that all three bias orientation have useful properties. We assumed a feed point at (0,-0.3) cm relative to the center of the patch. This was close to an edge and thereby resulted in a rather high resonant resistance. This feed point can be moved closer to the center of the patch to reduce the resonant resistance for matching purposes.

We varied the bias field strength to verify the resonant frequency tuning reported in Pozar's paper. Our results agreed with the reported data (specifically, Figure 2 of Pozar's paper which is reproduced below as Figure G-1) within a small frequency shift. Typically such shifts can be reduced by increased sampling of the geometry volume; however, for our purposes, our results agreed with Pozar's to a sufficient degree.

For the remainder of this section, we assume a bias field strength of 400 Oe.

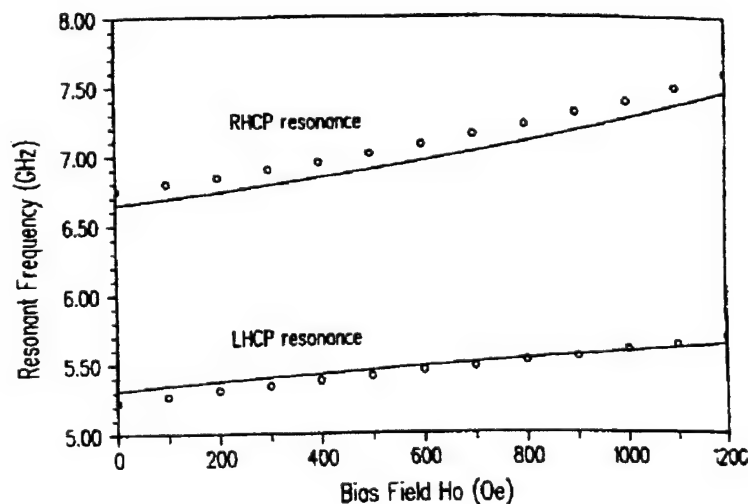


Figure G-1. Figure 2 from Pozar's paper [3]. This illustrates the variation of bias frequency as the bias field strength is changed for a normally biased ferrite-backed patch antenna.

G.1.1 Dielectric-backed Patch Antenna

MRC initially investigated the radiation properties of a dielectric-backed patch antenna with the same size as Pozar's antenna cited above and with a dielectric constant of 15. Figure G-2 illustrates the impedance spectrum of such an antenna.

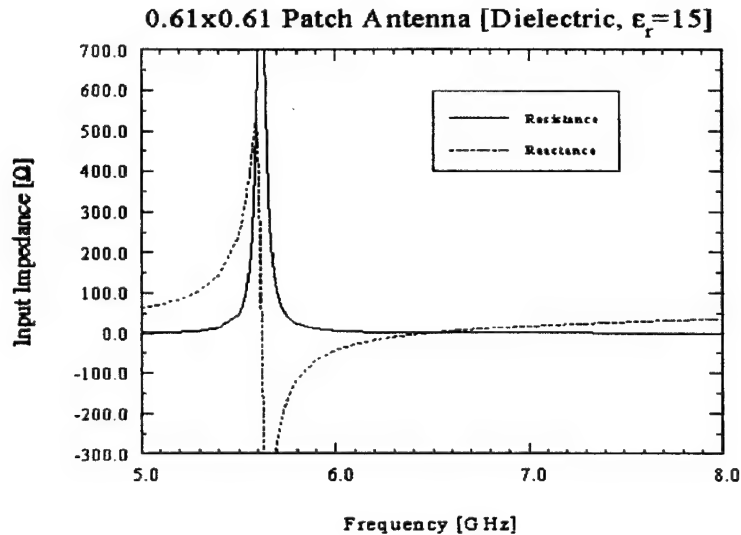


Figure G-2. Impedance spectrum of a 0.61x0.61 cm dielectric-backed patch antenna.

In Figure G-2, the dielectric-backed antenna is linearly polarized in the y-direction. Had we fed this antenna at (-0.3,0.0) cm rather than (0.0,-0.3), we would expect similar results; however, the radiation would now be polarized in the x-direction.

G.1.2 X-axis Ferrite Biasing

MRC modeled a ferrite-backed antenna where the bias orientation was along the x-axis (the bias field was 400 Oe). Figure G-3 illustrates the impedance spectrum for this antenna.

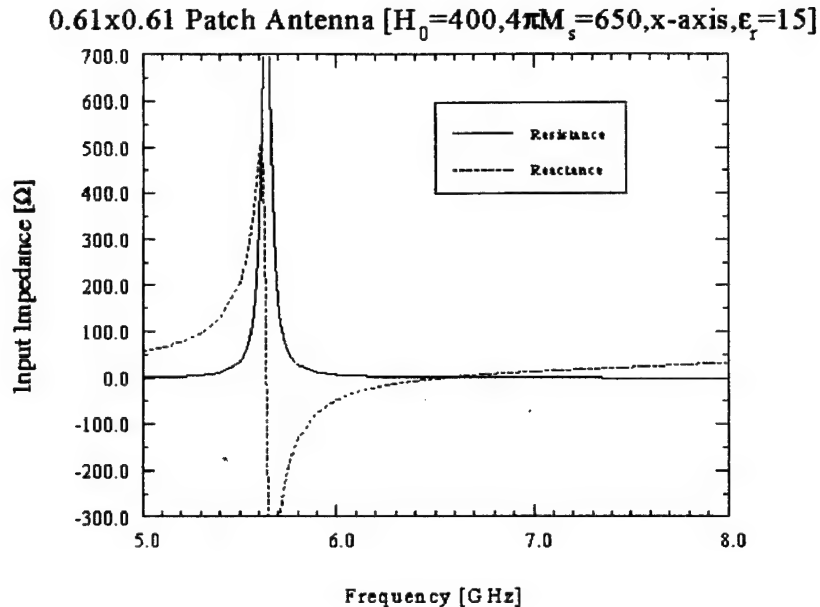


Figure G-3. Impedance spectrum for a 0.61x0.61 cm patch printed on a x-axis biased ferrite.

In this case, the resonant frequency was 5.65 GHz. Note that it resonates at a slightly higher frequency due to the application of a bias field. For a transversely biased ferrite, the polarization is linear and in this case the antenna is y-polarized.

G.1.3 Y-axis Ferrite Biasing

MRC modeled a ferrite-backed antenna where the bias orientation was along the y-axis (the bias field was 400 Oe). Figure G-4 illustrates the impedance spectrum for this antenna. In this case, the resonant frequency is 6.05 GHz. Notice the rather large shift in resonant frequency for this transverse bias orientation as compared to the dielectric (5.61 GHz) and the x-axis bias case (5.65 GHz). The radiation pattern is again linear and the radiated field is polarized in the y-direction. The cross-polarization term is asymmetric due to the position of the feed.

Note that for transversely biased antennas (e.g. x- or y-axis), the polarization is linear; however, the resonant frequency can be tuned over two ranges by varying the bias field. The two ranges are selected by the bias field orientation. In the cases presented herein, y-directed polarization was obtained by feeding the antenna along the y-axis. If we desire x-directed polarization, placing the feed on the x-axis would be appropriate.

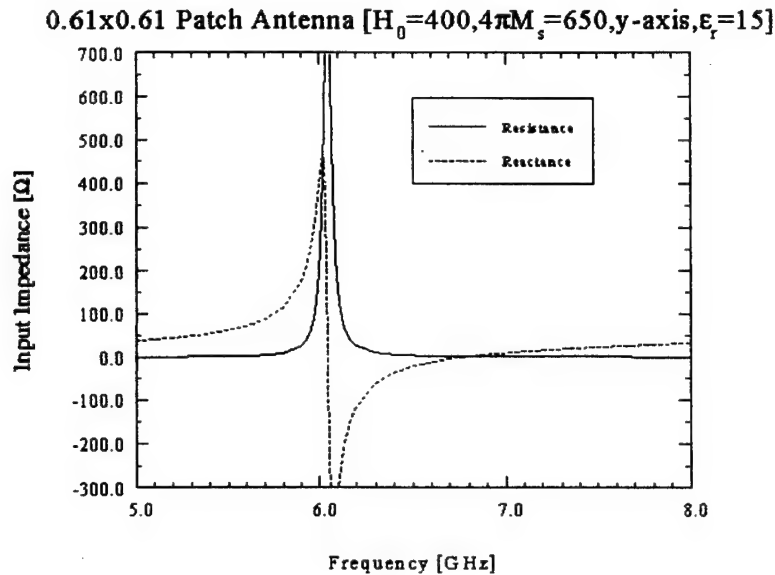


Figure G-4. Impedance spectrum of a 0.61x0.61 cm patch antenna on a y-biased ferrite.

G.1.4 Z-axis Ferrite Biasing

MRC modeled a ferrite-backed antenna where the bias orientation was along the z-axis (the bias field was 400 Oe). Figure G-5 illustrates the impedance spectrum for this antenna. In this case, two resonant frequencies are observed (as reported by Pozar and shown in Figure 1). One resonant frequency is at 5.115 GHz while the other is at 6.445 GHz.

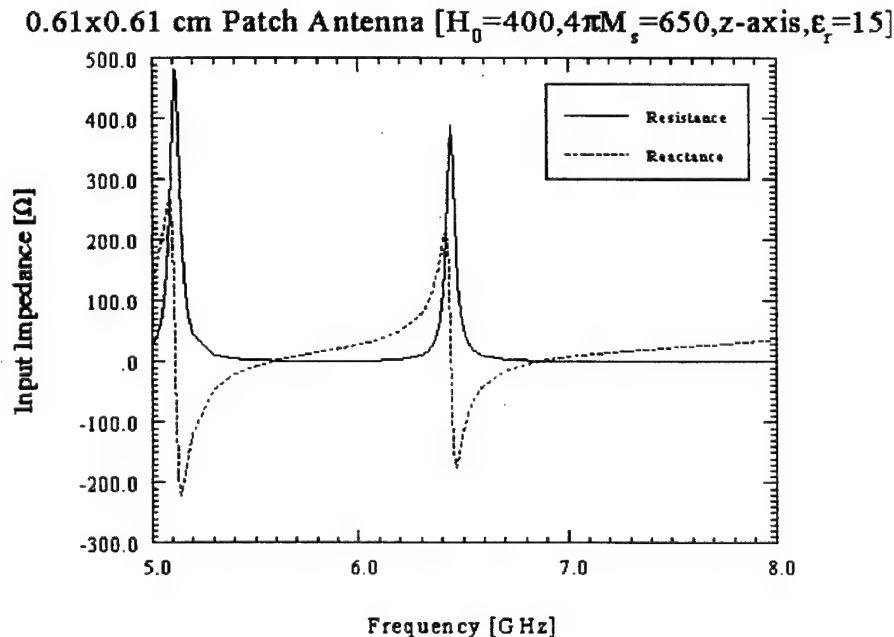


Figure G-5. Impedance spectrum for a 0.61x0.61 cm antenna on a normally biased ferrite.

The radiation pattern at 5.115 GHz is left-hand circular polarized (LHCP) and it is shown for the x- and y-axis cuts in Figure G-6. The corresponding pattern at 6.445 GHz, which is right-hand circular polarized (RHCP), is shown in Figure G-7.

0.61x0.61 cm Patch Antenna [$H_0=400, 4\pi M_s=650, z\text{-axis}, \epsilon_r=15$]

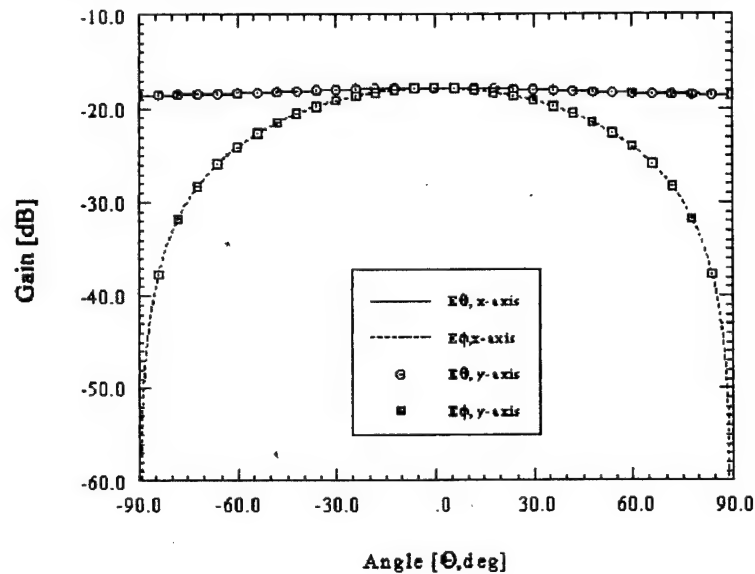


Figure G-6. Gain pattern for a normally biased patch antenna at 5.115 GHz.

0.61x0.61 cm Patch Antenna [$H_0=400, 4\pi M_s=650, z\text{-axis}, \epsilon_r=15$]

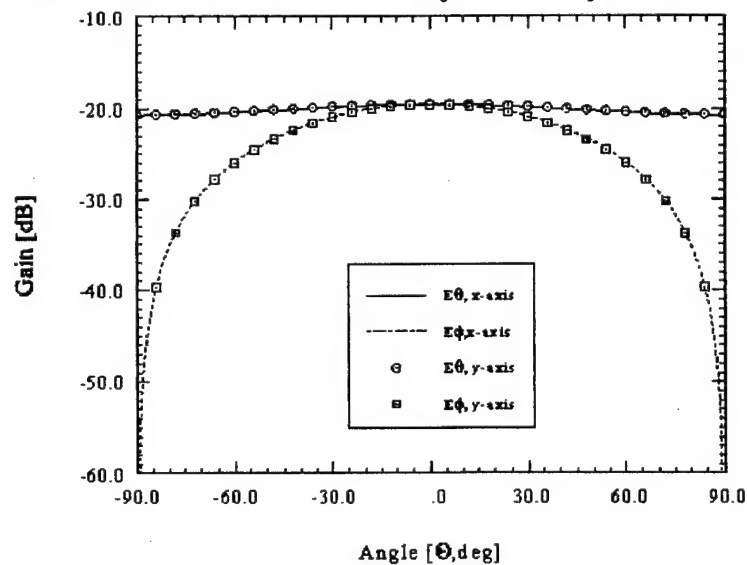


Figure G-7. Gain pattern for a normally biased patch antenna at 6.445 GHz.

G.1.5 Summary of Radiation Simulations

Clearly, a normally biased antenna can be operated in one of two circular polarization modes at two distinct frequencies. Also, linear polarization is obtained when the bias field is transverse to the ferrite (again at two distinct frequencies). Fine frequency tuning can be accomplished by varying the bias field strength.

These results suggest that a polarization and frequency diverse square antenna element can be obtained by providing two feed points (one along the x-axis, one along the y-axis) only one of which is excited for a desired polarization. A means of the bias field strength and orientation must be provided perhaps through the use of small electromagnets. This antenna, with no moving parts, would be capable of various linear polarization states as well as a circular polarization mode. It would also be capable of operating over a large bandwidth by altering the bias field direction and strength even though the instantaneous bandwidth is quite small. MRC is currently investigating the use of two feeds at the same time; however, the feeds are fed 90 degrees out-of-phase. We anticipate circular polarization for the dielectric and z-axis biased ferrite while the x- and y-axis biased ferrite configurations will remain linearly polarized. This is due to the fact that the two feed points in the case of x- or y-biased ferrite patch antennas excite different antenna resonances and hence at most only one feed or the other will be "active" (e.g. matched) and any given frequency.

G.2 Large Ferrite-backed Antenna Array

MRC modeled a 11 x 11 patch antenna array on a Silicon Graphics workstation using only 60 MB of RAM and double precision calculations. Each antenna element was 4 x 3 cm and placed on top of a 8 x 6 x 0.15 cm ferrite slab (within a metal cavity). The center-to-center element spacing was 10 cm in both directions yielding a total array size of approximately 1 x 1 meter and resulting number of unknowns was approximately 50,000. The gain pattern for this antenna is shown in Figure G-8. In this, the main lobe was steered to 30 degrees off broadside using standard beam steering techniques. Computation of this pattern required approximately 8.5 hours on a Silicon Graphics workstation.

To model a similar antenna using a second-order ABC and brick elements, MRC estimates approximately 775,000 unknowns (ABC is five layers from antenna + 50,000 unknowns for the antenna itself). Clearly, such an explosive growth in the number of unknowns is not conducive to accurate and efficient solution. Assuming an average bandwidth of 60, a direct solver used in a FE-ABC computer program would require approximately 744 MB of RAM before fill-in! We note that for similar zoning, the number of unknowns in a tetrahedral mesh will be higher than the brick mesh cited above.

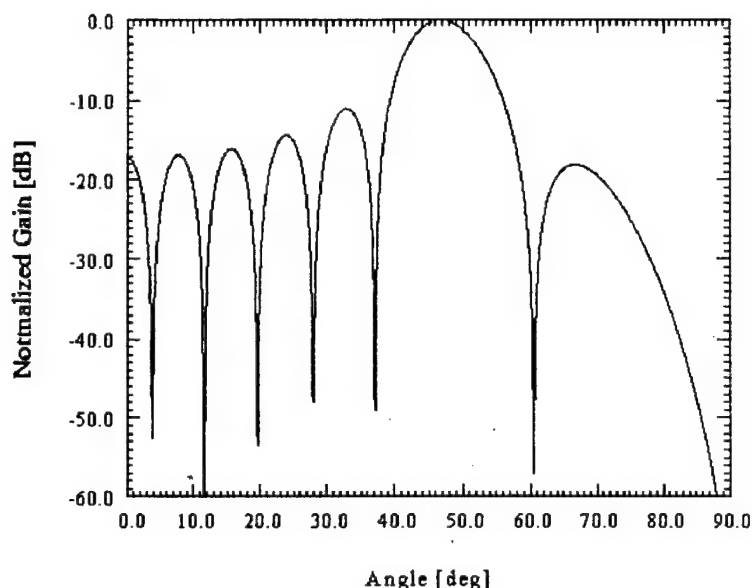


Figure G-8. Radiation pattern from an 11 x 11 array of patch antennas printed on a ferrite substrate. *This example illustrates MRC's ability to model large structures on ferrite materials including antenna elements and phase shifting devices.*

H. Non-Uniform Static Bias Field Effects

Practical ferrite antenna construction often involves a permanent magnet to provide the required static magnetic bias field. Most CEM analysis techniques for ferrite material (in particular the method of moments) assume implicitly a uniform bias field distribution. However, since permanent magnets are finite, the static field attributed to them is non-uniform. Figure H-1 illustrates the static magnetic field within a metallic cavity as measured by Dr. Kokotoff [2]. Note that the field has roughly a parabolic shape and that introduction of steel bars between the magnet and the ferrite-filled cavity reduces the distortion in the static field. Also, as the static field increases (here by use of more permanent magnets), the "bowing" in the static field becomes more distinct.

The non-uniform field encountered in practice encourages the use of the finite element method *since the non-uniform bias field results in an magnetically inhomogeneous ferrite sample.*

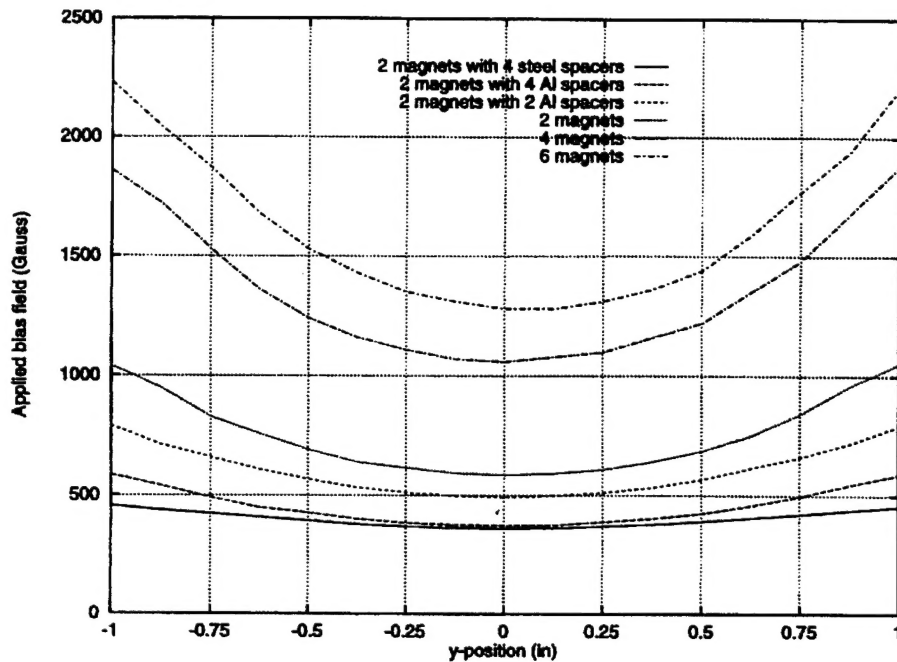


Figure H-1. Measured magnetic field distribution within cavity from [2].

As an example of the effect of a non-uniform bias field, consider the scattering by a 6 cm x 6 cm x 1 cm ferrite filled cavity. Figure H-2 illustrates the variation in RCS as a function of frequency and non-uniform bias state. Note that the RCS near 1.5 GHz is prominently affected by the bias field distribution throughout the cavity.

RCS of a 6x6x1 cm Cavity w/ Various Biasing Schemes

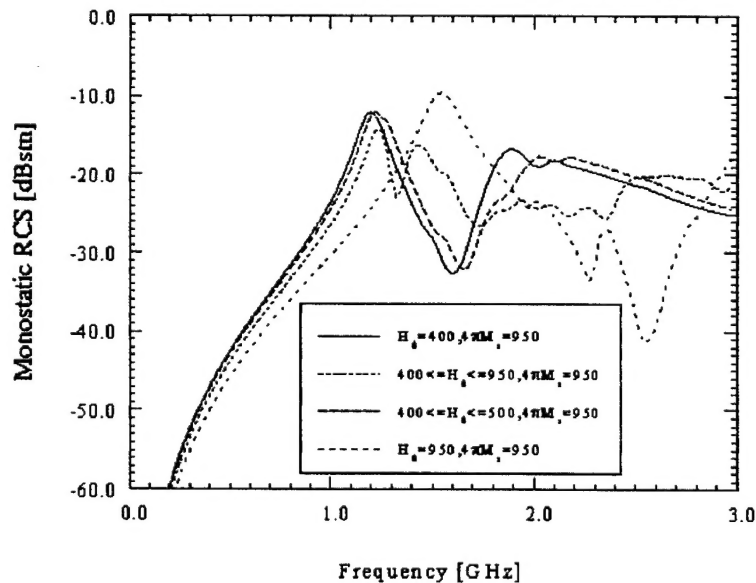


Figure H-2. Illustration of non-uniform bias field effect on the RCS of a ferrite-filled cavity.

This example demonstrates the requirement for a finite element computer program since MoM cannot model non-uniform bias fields. Further examples of the importance of including non-uniform bias fields will be presented in Section I.

I. Ferrite Radomes: An Electronic Shutter Concept

An important proposed application of ferrite materials is as a radome. This is due to the fact that the magnetically tunable properties (loss and effective permeability) are potentially useful as an electronic shutter. Typically, radomes are designed to permit radiation from the antenna to the outside world either at all frequencies (a dielectric radome) or in a limited band of frequencies using a frequency selective surface (FSS). Unfortunately, the reality of physics is that a good antenna is a good scattering body and hence if a radome is transparent, the RCS of the antenna can be a significant factor in the over-all platform RCS. Hence a need to shutter the radome and make it transparent only during active radiation.

MRC undertook at the end of Phase I a brief feasibility study concerning the use of ferrites as an electronic shutter. The results are somewhat promising. The ferrite layer does indeed act like a shutter radome, though it is very narrow banded. A solution for this narrow bandwidth of operation should become an active research topic in order to utilize ferrites as shutter radomes. This section presents MRC's investigation of ferrite radomes beginning with the modified FE-BI computer program necessary for determining the transmission coefficient of a ferrite sample.

I.1 Two Aperture FE-BI Computer Program for Transmission Calculations

MRC modified the FE-BI computer program discussed in Section B. This modification consisted of opening an aperture at the base of the metallic cavity and hence providing the capability of modeling thick metallic planes. The boundary integral submatrix could be re-used since the discretization is identical for the upper and lower apertures when brick elements are used in the volume. This computer program requires a few more unknowns but no new calculation or storage of the matrix entries hence its efficiency is comparable to the single aperture brick FE-BI computer program.

I.2 Transmission Coefficient Calculations

The transmission coefficient for a ferrite sample was calculated by first computing the far-zone forward scattered fields when the volume between the apertures is filled with air. Then the forward scattered fields are computed with the ferrite material in the cavity. The transmission coefficient was then calculated by dividing the latter by the former

$$T = \frac{E_{\phi,\theta}^{\text{filled}}}{E_{\phi,\theta}^{\text{empty}}} \quad (41)$$

where the fields are complex and the division is done on a component-by-component basis. This scheme removes the fixture scattering (e.g. thick metal plane with an aperture) from the calculation to isolate the ferrite effects. Figure I-1 illustrates the transmission coefficient for a ferrite sample with various uniform and non-uniform bias field distributions.

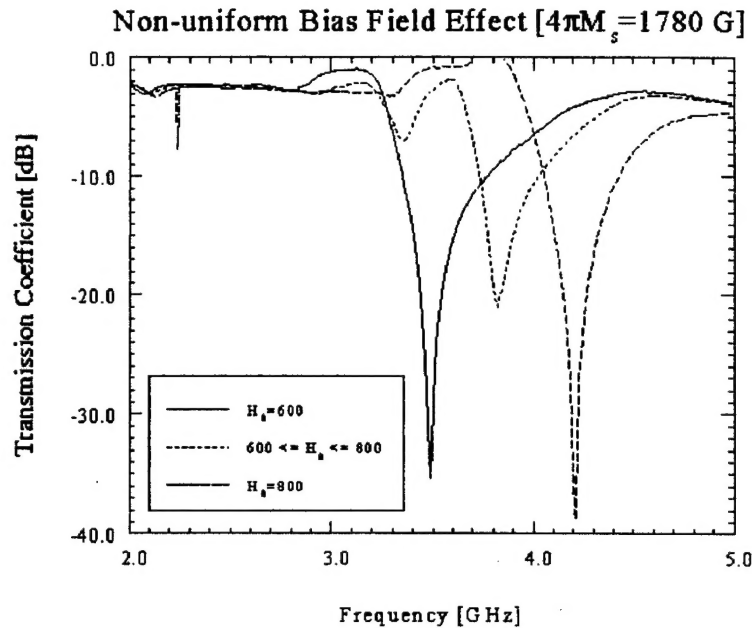


Figure I-1. Transmission coefficient for a ferrite substrate under various bias conditions.

Clearly, the transmission coefficient is determined by the bias field and a non-uniform bias field has an effect. The transmission null (e.g. when the radome is opaque) is a characteristic of ferrites and its location is determined by the ferrite material properties and bias field distribution.

J. Concluding Remarks and Suggestions for Future Work

During Phase I of this SBIR effort, MRC and UM demonstrated the feasibility of using modern finite element analysis to characterize the behavior of ferrite materials. Specifically, MRC and UM investigated the following:

1. Finite element formulations for ferrite materials.
2. Implementation of those formulas in a computer program.
3. Convergence issues when ferrite materials are being modeled.
4. Mesh truncation schemes.
5. Element distortion effects.
6. and uses of ferrite antennas as frequency-agile antennas, polarization-agile antennas and electronic shutter radomes.

The importance of these studies will be realized in Phase II as the MRC Team develops a state-of-the-art conformal ferrite antenna modeling package.

J.1 Suggestions for Future Work

The MRC Team suggests the following engineering services relating to finite element analysis research and development be performed:

1. Modify existing Phase I brick finite element program to incorporated advances made during Phase II in terms of iterative equation solvers or optimization techniques.

2. Develop a tetrahedral finite element program capable of modeling ferrites, dielectrics, and perfect electric conductors.
3. Develop models of the static magnetic field within the antenna cavity to include non-uniform bias field effects.
4. Develop user-oriented antenna design tools that incorporate advanced frequency extrapolation and antenna optimization features.
5. Investigate improved matrix solution algorithms.
6. Investigate improved (more flexible) mesh truncation schemes.
7. Investigate ferrite antenna uses through a combination of modeling, prototype fabrication, and measurement.
8. Investigate novel ferrite-based feed networks that will offer advantages in terms of size, weight, and reduced complexity as compared to current phased array feed networks.

K. References

¹ D.M. Pozar, Microwave Engineering, New York: Addison-Wesley, 1990.

² D. M. Kokotoff, "Full-wave analysis of ferrite-tuned cavity-backed antenna," Ph.D. Dissertation, Arizona State University, 1995.

³ David M. Pozar, "Radiation and scattering characteristics of microstrip antennas on normally biased ferrite substrates," *IEEE Trans. Antennas Propagat.*, **40**, Sept. 1992, pp. 1084-1092.

⁴ Z.S. Sacks, D.M. Kingsland, R. Lee, and J.F. Lee, "A perfectly matched anisotropic absorber for use as an absorbing boundary condition," *IEEE Trans. Antennas Propagat.*, **43**, pp. 1460-1463, Dec. 1995